Low-order dynamical system model of a fully-developed turbulent channel flow

Nicholas Hamilton,[1] Murat Tutkun,[2,3] and Raúl Bayoán Cal[1]

[1] *Portland State University, Department of Mechanical and Materials Engineering, Portland, OR 97202, USA*
[2] *IFE, Department of Process and Fluid Flow Technology, 2007 Kjeller, Norway*
[3] *University of Oslo, Department of Mathematics, Blindern 0316 Oslo, Norway*

(Dated: May 15, 2017)

A reduced order model of a channel flow is composed from direct numerical simulation data obtained from the turbulence database hosted at Johns Hopkins University. Snapshot proper orthogonal decomposition (POD) is used to identify the Hilbert space from which the reduced order model is obtained, as the POD basis is defined to capture the optimal energy content by mode. The reduced order model is defined by coupling the evolution of the dynamic POD mode coefficients through their respective time derivative with a least-squares polynomial fit of terms up to cubic order. Parameters coupling the dynamics of the POD basis are defined in analog to those produced in the classical Galerkin projection. The resulting low-order dynamical system is tested for a range of basis modes demonstrating that non-linear mode interactions do not lead to a monotonic decrease in error propagation. A basis of five POD modes accounts for 50% of the integrated turbulence kinetic energy but captures only the largest features of the turbulence in the channel flow and is not able to reflect the anticipated flow dynamics. Using five modes, the low-order model is unable to accurately reproduce Reynolds stresses and root-mean-square error of the predicted stresses is as great as 30%. Increasing the basis to 28 modes accounts for 90% of the kinetic energy and adds intermediate scales to the dynamical system. Difference between the time derivatives of the mode coefficients and their least-squares fit is amplified in the numerical integration leading to unstable long-time solutions. Periodic recalibration of the dynamical system is undertaken by limiting the integration time to the range of the sampled data and offering the dynamical system new initial conditions. Renewed initial conditions are found by pushing the mode coefficients in the end of the integration time toward a known point along the original trajectories identified through a least-squares projection. Under the recalibration scheme, the integration time of the dynamical system can be extended to arbitrarily large values provided that modified initial conditions are offered to the system. The low-order dynamical system composed with 28 modes employing periodic recalibration reconstructs the spatially averaged Reynolds stresses with similar accuracy as the POD-based turbulence description. Data-driven reduced order models like the one undertaken here are widely implemented for control applications, derive all necessary parameters directly from the input, and compute predictions of system dynamics efficiently. Speed, flexibility, and portability of the reduced order model come at the cost of strict data requirements; the model identification requires simultaneous realizations of mode coefficients and their time derivatives, which may be difficult to achieve in many investigations.

I. INTRODUCTION

Reduced order modeling describes a wide range of approaches that approximate complex system dynamics of large or infinite degrees of freedom with a limited number of degrees of freedom. For applications in turbulence, the goal is typically to simplify the Navier-Stokes (NS) equations, by isolating the important dynamics for a given flow with an effective use of computational resources. Of these approaches, modal decomposition methods are frequently selected as they add definition and organization to the vector space of the input information and offer intuitive means of filtering or truncation. The proper orthogonal decomposition (POD) is a widely-used method as it represents the optimal organization of turbulence structures based on energy [1]. Careful selection of the point of truncation of the mode basis retains the greatest range of dynamics in the system with the least number of modes [2]. For turbulent flow data of high spatial resolution, the classical POD presented by Lumley [3] is not as computationally efficient as the method of snapshots as per Sirovich [4].

An attractive extension of the POD for dynamical system modeling, the Galerkin projection, is widely used to reconcile the modal basis with a governing behavior law, resulting in a minimal set of ordinary differential equations [5]. The Galerkin-POD procedure was first used in turbulent shear flow modeling by Aubry et al. [6], and has since been extended to many flow scenarios; e.g. mixing layers and wakes [7, 8], compressible flows [9], and bluff body wakes and aerodynamics [10, 11]. However, the ability of the POD to represent the dynamics of a system is quite sensitive to transient behavior; deviations of the system from the reference frame of the POD quickly result in divergence of the low-order dynamical system (LODS) [12–15]. Galerkin-POD models offer great potential in computations of complex dynamics given that closure assumptions can be provided. Recent work in Galerkin-POD reduced order models focus on accounting for additional turbulence terms, such as eddy viscosities [10, 16, 17] and diffusion models to keep the system stable. Adding extra terms to reduced order models increases stability for long integration periods, mostly due to dissipation, and balancing the dynamics included in the coherent POD modes [10].

Unstable reduced order models derived from the Galerkin-POD method have been combined with correction factors in order to keep the dynamics within the bounds of the original system. Such corrections can be quite effective at introducing stability, but risk suppressing complexity of the system [8]. Stability may also be introduced by treatment of the pressure term as pointed out by Noack et al. [14] and Rempfer [2] and is especially important in compressible flow applications such as acoustic fields and transonic flows [18]. Flows in which the fluctuating pressure does not have a large effect typically do not gain much from the inclusion of pressure in the Galerkin system. Another constraint in the Galerkin projection is that a large database is necessary to compute the inner products and spatial gradients of constituent modes to sufficient statistical convergence. Consequently, LODS are most effectively derived from numerical simulation data or require strong closure assumptions, particularly in an experimental framework [7, 19]. A comprehensive history of closure problems for dynamical modeling of turbulence is provided in Brunton and Noack [20]

The amount of data required to define a reduced order model is often a difficult constraint to overcome, and may defeat the purpose of seeking the low-dimensional system. An analogous approach to the Galerkin-POD method was presented in Perret et al. [21] wherein the dynamic mode coefficients, rather than the spatially coherent modes, are used directly in the formation of the dynamical system. In this approach, simultaneous realizations of the coefficients and their respective time derivatives are required to resolve the evolution of the system. The derivatives of the coefficients are combined through a least-squares polynomial fit including constant, linear, quadratic, and cubic parameters. Linear and quadratic parameters are analogous to those produced through the Galerkin-POD method accounting for mode interaction in the viscous and convective terms of the Navier-Stokes equations. Constant and cubic parameters added to the LODS through the least-squares polynomial fit do not issue from projection of the behavior law, but can add stability to the resulting dynamical system [7].

While data-driven (empirical, black-box) dynamical models are not as common for applications in turbulence as the Galerkin-POD or other methods built on the Navier-Stokes equations, they offer promising possibilities for flow control and prediction applications. Even though models like the polynomial fit method do not explicitly require knowledge of the underlying physics, they offers several advantages in terms of ease of definition of dynamics, speed of calculation, and portability to control methods [22]. Because computational costs are often low for data-driven models, composition with a larger range of POD modes is feasible, and account for a broader range of system dynamics [23–25]. Auxiliary turbulence terms and physical mechanisms sought in numerous Galerkin-POD studies [10, 16, 17] are taken implicitly from the dynamics of the input data in this application. Data-driven methods that do not require knowledge of the underlying physics

ingly also be classified as model-free systems. By definition, data-driven modeling methods seek system dynamics from the input or training data and so may be applied to any dynamical system, without regard of the governing behavior law.

Numerical solution of ordinary differential equations often leads to the propagation of error that can rapidly accumulate and cause divergence of the system. This is a common issue in POD based dynamical systems. Often, exclusion of higher order modes that account for dissipation and diffusion mechanisms [26] changes the energy balance of the system. Other potential pitfalls with POD based systems are incompletely converged basis modes, and sensitivity to initial conditions [20], which can lead to skewed descriptions of the flow field. Error propagation in reduced order models has been reduced through a number of recalibration techniques (e.g. [16, 27–31]). Recalibration has been successfully employed for a wide range of dynamical systems, including model-free and purely empirical models.

A low-order dynamical system evolving from the proper orthogonal decomposition is explored for a small sample of the direct numerical simulation of a fully-developed turbulent channel flow hosted at Johns Hopkins University [32]. By reducing the spatial and temporal range of the sample, the resulting LODS is given incomplete information on the dynamics. It is of interest to determine how well a dynamical system approximates the dynamics of the full system with limited training data. The channel flow is a fundamental turbulence case that has been explored numerically and experimentally to a great extent. Because the flow is well-studied within the range of Reynolds numbers tested, it represents an opportunity for development of reduced order modeling techniques. To date, DNS remains too expensive for direct control applications, making reduced order modeling techniques a necessary intermediary for flow and aerodynamic control. Low-order models explored below require between 5 and 30 degrees of freedom, opening the possibility for future flow control applications. Error propagation within the dynamical system is tested as a function of the number of modes used to compose the least-squares polynomial fit. The LODS is subjected to iterative recalibration by periodically halting the integration of the ordinary differential equations (ODEs) and offering new initial conditions found by minimizing the error between the vector of predicted mode coefficients and their counterparts from the POD. The recalibration further requires that the coefficients be continuous and differentiable across the recalibration, preventing sudden changes in the predicted velocity fields.

II. THEORY

A. Snapshot proper orthogonal decomposition

The method of snapshots was modified from the original POD as a means of reducing the computational cost for input data with fine spatial resolution. The development follows that proposed by Sirovich [4] providing an ordered set of modes and associated eigenvalues delineating the energy associated with each mode. Below, bold math symbols represent vectorial quantities and symbols in plain text are scalar quantities. The flow field is assumed to be a stochastic function of space and time. Velocity snapshots are then denoted as $\boldsymbol{u}(\boldsymbol{x}, t^n)$, where $\boldsymbol{x}$ and t^n refer to the spatial coordinate and time at sample n, respectively, over N total snapshots $t^0 \leq t^n \leq t^N$.

The POD seeks to decompose the fluctuating velocity field into a modal basis of the form,

$$\boldsymbol{u}(\boldsymbol{x}, t) = \sum_{i=1}^{N} a_i(t)\boldsymbol{\Phi}^{(i)}(\boldsymbol{x}). \tag{1}$$

In equation (1), it is proposed that the velocity can be represented as the superposition of modes $\boldsymbol{\Phi}^{(i)}(\boldsymbol{x})$ that communicate spatial organization and time-varying coefficients $a_i(t)$. By convention in the snapshot POD, the modes themselves carry no units. It is only in combination with their respective coefficients that they represent contributions to the velocity field.

The POD modes are sought through solution of a Fredholm integral equation of the second kind,

$$\int_{\Omega} \boldsymbol{R}(\boldsymbol{x}, \boldsymbol{x}')\boldsymbol{\Phi}(\boldsymbol{x}')d\boldsymbol{x}' = \lambda\boldsymbol{\Phi}(\boldsymbol{x}), \tag{2}$$

where $\boldsymbol{R}(\boldsymbol{x}, \boldsymbol{x}')$ is the two-point spatial correlation tensor, Ω is the physical measurement domain, and λ are eigenvalues that delineate the integrated turbulence kinetic energy associated with each POD mode.

Equation (2) is discretized to be solved numerically and modes are computed by projecting the snapshot basis into the eigenvector space in product with a vector of coefficients $\mathcal{A}^i(t^n)$. Modes are normalized by their respective L^2-norms forming an orthonormal basis as,

$$\mathbf{\Phi}^{(i)}(\boldsymbol{x}) = \frac{\sum_{n=1}^{N} \mathcal{A}^i(t^n)\boldsymbol{u}(\boldsymbol{x},t^n)}{\| \sum_{n=1}^{N} \mathcal{A}^i(t^n)\boldsymbol{u}(\boldsymbol{x},t^n)\|}, \qquad i = 1, ..., N. \tag{3}$$

Coefficients $a_i(t)$ in equation (1) are found by back-projecting the set of stochastic velocity fields onto the basis of POD modes and integrating over the domain,

$$a_i(t) = \int_{\Omega} \boldsymbol{u}(\boldsymbol{x},t)\mathbf{\Phi}^{(i)}(\boldsymbol{x})d\boldsymbol{x}. \tag{4}$$

Reconstruction with a limited set of POD modes results in a filtered description of the input snapshot basis. As the POD seeks the energy carrying turbulent structures, accounting for the greatest common projection of the kernel, low-rank modes are taken to be the most energetic and least isotropic structures in the flow field. Intermediate and high-rank POD modes account for turbulence kinetic energy that is more homogeneously distributed and more isotropic, as detailed in Hamilton et al. [33]. The truncation point of the POD mode basis is often determined by setting a threshold of the energy described by the POD eigenvalues, λ.

B. Least squares polynomial fit

An alternate approach to formulating a dynamical system from the POD follows the method of Perret et al. [21]. There, the dynamical system was proposed following a polynomial expansion of permutations of the POD coefficients. A POD basis is truncated to N_r modes, and the coefficients are combined as,

$$\frac{da_i}{dt} = D_i + \sum_{j=1}^{N_r} L_{ij}a_j + \sum_{j,k=1}^{N_r} Q_{ijk}a_j a_k + \sum_{j,k,l=1}^{N_r} C_{ijkl}a_j a_k a_l. \tag{5}$$

In equation (5), the parameters arise from least squares fit of monomial terms onto the time derivative of the POD coefficients directly, rather than projecting the governing behavior law onto the POD basis. No additional regularization was implemented in calculating the LODS parameters beyond the normalization of the data and of the POD modes as detailed in equation (3). The parameters sought are D_i, L_{ij}, Q_{ijk}, and C_{ijkl}, relating for constant, linear, quadratic, and cubic mode interaction, respectively. Parameters are calculated iteratively for each input mode i and involve many terms [21]. Each index i, j, k, l spans the POD basis selected.

A more consolidated form of the dynamical system is,

$$\frac{da_i}{dt} = \sum_{k=1}^{N} x_k A_k(a_1, ..., a_{N_r}), \tag{6}$$

where x_k are the unknown parameters and A_k are the monomial terms at most cubic. There are a total of N_p parameters that couple the mode coefficients, found by minimizing the error function,

$$\chi^2 = \sum_{p=1}^{N} \left[\frac{da_i}{dt} - \sum_{k=1}^{N} x_k A_k(a_1(t_p), ..., a_{N_r}(t_p)) \right]^2. \tag{7}$$

Minimization is accomplished numerically by $\chi^2 = |AX - B|^2$, where X is the vector of unknown coefficients, B the vector containing the N samples of da_i/dt and A the matrix of terms $a_j(t_p)$, $a_j(t_p)a_k(t_p)$, and $a_j(t_p)a_k(t_p)a_l(t_p)$. In the definition of the coupled set of ordinary differential equations (ODEs) in equation (5), the POD modes themselves are not employed in the calculating the behavior of the system. One main advantage is that this approach includes cubic terms which are known to add complexity to the system without introducing instability [7, 19, 21].

A potential detriment to large mode bases is that the system requires that a large number of parameters be calculated. The total number of parameters calculated is then $N_p = N_r + N_r^2 + N_r^3 + N_r^4$, for the constant, linear, quadratic, and cubic terms coupling each mode to every other mode in the basis. The system requires that there be records of both a_i and da_i/dt. This constraint is not insurmountable with direct numerical and large eddy simulations, but poses a challenge for many experimental approaches.

Numerical solution of the ODEs in equation (5) results in a new time series of coefficients predicting the relative intensities of each of the modes forming the LODS. Any quantity issuing from the POD dynamical system will be denoted below with a caret ($\hat{}$). The least-squares fit of the time derivatives of the POD coefficients is written $d\hat{a}_i/dt$, the mode coefficients from the LODS are $\hat{a}_i$, and are a function of a new vector of time values $\hat{t}$. The time resolution of $\hat{a}_i(\hat{t})$ is related to the error tolerance of the numerical ODE solver and the number of modes in the system [21, 27].

III. TURBULENT CHANNEL FLOW DIRECT NUMERICAL SIMULATION

An overview of the direct numerical simulation (DNS) of a fully-developed channel flow hosted at Johns Hopkins University (JHU) is provided here with particular attention paid to the sample data extracted from the simulation and used in the following analysis. For a complete description of the procedure and simulation, the reader is referred to the documentation provided by JHU [32] (see also, [34, 35]). Here, focus is placed on interpretation the POD and reduced order models. Accordingly, a relatively small sample of the full channel flow is selected, limiting both the spatial and temporal ranges of the data.

The channel flow DNS uses periodic boundary conditions in both the streamwise and spanwise directions and no-slip boundary conditions at the walls. The Navier-Stokes equations are solved using a wall-normal velocity-vorticity formulation [36], according to which solutions are provided using a Fourier-Galerkin pseudo-spectral method for the streamwise and spanwise directions and seventh-order Basis-splines (B-splines) collocation method in the wall normal direction. Time integration is performed using a third-order Runge-Kutta method. The simulation was performed using the petascale DNS channel flow code (PoongBack) [37]. The simulation is performed for approximately a single flow through time of 26 non-dimensional time units, obtained with the streamwise length of the domain $8\pi H$ and a bulk flow velocity of 0.99994. The Reynolds number of the flow based on the outer scaling is $Re_b = U_b 2H/\nu = 3.9998 \times 10^4$; the complementary friction velocity Reynolds number is $Re_\tau = u_\tau H/\nu = 9.9935 \times 10^2$.

Data sampled from the full DNS and discussed below represent a small subset of the total provided in the database. Data spans the channel half-height, $-1 \leq y/H \leq 0$ (normalized by the channel half-height H). Measurement points were selected in the wall-normal direction by taking every fourth point from the full resolution of the DNS. Resolution of the data in the streamwise direction is set to $\Delta x/H = 0.0123$ and in the spanwise direction to $\Delta z/H = 0.0061$. A total of 512 snapshots were sampled from the channel flow, representing a small portion of the full simulation time, $t \in [0, 3.32]$. Parameters of the sampled data are summarized in Table I, and visualized in the schematic in Fig. 1(a). Coordinates shown in the table are normalized by the channel half-height H; velocities are normalized by the bulk fluid velocity U_b; time resolution is normalized by H/U_b. Turbulence seen in the central region of the channel is expected to exhibit the passage of large, anisotropic structures, although in an ensemble sense, the turbulence in the outer layers is more isotropic. The half-channel velocity profile is shown in viscous units in Fig. 1(b).

TABLE I. Details of sampled volume data.

spacing in $x-$direction	$\Delta x = 12.3$
spacing in $y-$direction	$0.0016 \leq \Delta y \leq 6.2$
spacing in $z-$direction	$\Delta z = 6.1$
time resolution between snapshots	$\Delta t = 0.0065$
measurement points	$n_x \times n_y \times n_z = 32 \times 64 \times 32$
number of snapshots	$n_t = 512$

Ensemble-averaged mean velocities are shown in Fig. 2. Full resolution of the channel to this depth is represented by more than 256 points; significant down-sampling has occurred in the presented snapshots and is evident in the contours of the volume shown for mean velocities. Downsampling in this way limits the range of dynamics present in the dataset to a subset of the full DNS. The mean flow field in the channel shows a streamwise velocity two orders of magnitude larger than the wall-normal and spanwise components.

This manuscript was accepted by Phys. Fluids. Click here to see the version of record.

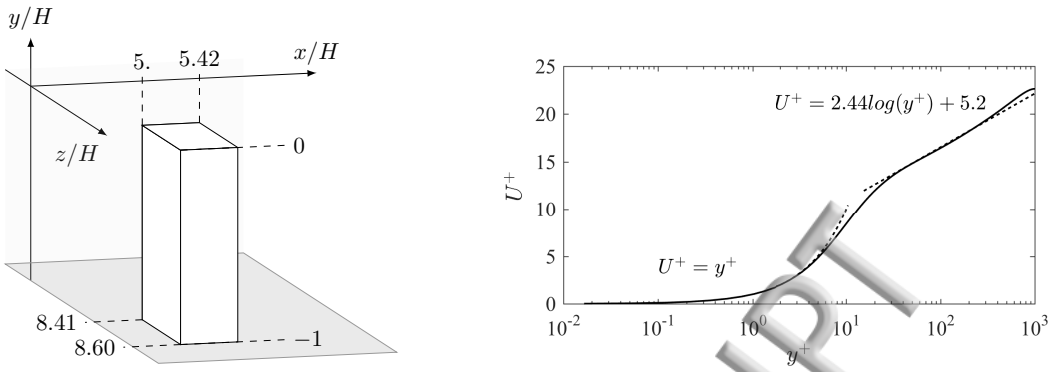

(a)Schematic of the lower half of the channel flow DNS simulation space. Sample volume was sized to span from the wall to the centerline of the channel

(b)Half-channel velocity profile shown in inner scaling. Dashed lines correspond to the viscous sublayer and the log-layer.

FIG. 1. Schematics indicating the sampled data in the channel and the velocity shown in viscous wall units.

Accordingly for wall-bounded flows, the high-shear region is confined to the near-wall region. The magnitude of U rapidly increases below $y/H \leq -0.8$ and changes little toward the center of the channel. Spanwise variations remain in the ensemble averaged velocity field, reflecting the down-sampling of the dataset. In the full DNS, the mean wall-normal and spanwise velocities approach zero. Although the magnitudes of V and W are very small compared to U, some features remain in Figs. 2(b) and 2(c) that are representative of the data sample, but differ from the spatially-averaged statistics of the full DNS.

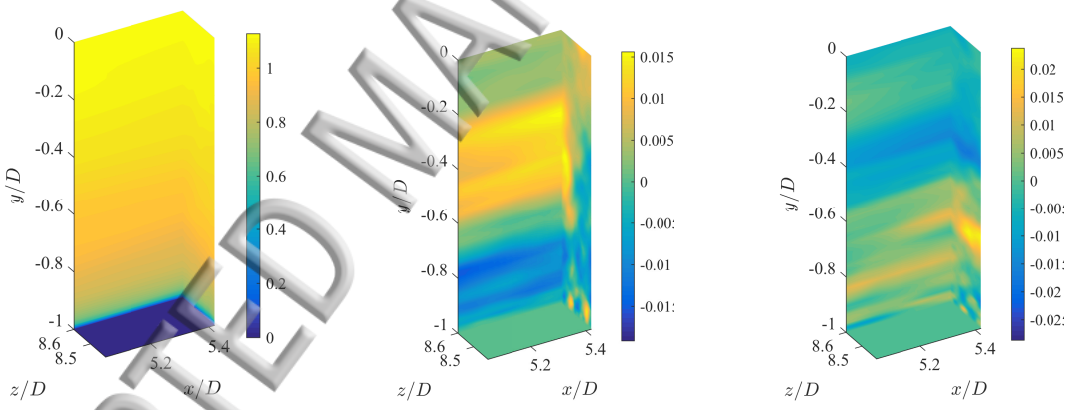

(a)U (b)V (c)W

FIG. 2. Streamwise, wall-normal, and spanwise mean velocities in channel flow scaled by the bulk velocity.

Turbulence in the sampled data is the field of interest in the development of the following dynamical system. Fig. 3 shows the turbulence kinetic energy ($k = \overline{u_i u_i}/2$) and several turbulent stresses, averaged only in time. Stress fields in the figure are used as the basis for comparison for the POD representations of the flow field and LODS below. Streaks are evident near the wall, shown in both k and $\overline{uv}$, as well as a larger structure in the lower-right corner of the sampled volume. Larger structures of lower magnitude are seen toward the center of the channel. Systems with a large range of structures that are significant to the flow dynamics are notoriously difficult to capture with POD based modeling approaches due to the number of modes that must be retained in the flow description. Wall-normal and spanwise normal stresses are smaller in magnitude than $\overline{uu}$ but show similar size and distribution of turbulence structures. Streaks near the wall as seen in k (Fig. 3(a)) arise from contributions of the streamwise and spanwise normal stresses but are absent in $\overline{vv}$.

The streamwise/wall-normal Reynolds shear stress $\overline{uv}$ (Fig. 3(c)) is the only off-diagonal term from the turbulence stress tensor expected to have a non-null profile in statistics from the full DNS. The figure

shows several regions of large magnitude below $y/H \leq -0.8$; away from the wall $\overline{uv}$ is comparatively small. According to symmetry in the channel flow, it is expected that $\overline{uw}$ and $\overline{vw}$ tend toward zero with complete statistical convergence; because the sample analyzed here spans a relatively small space and time interval of the DNS, stresses including fluctuations in the spanwise direction exhibit features on the same order as $\overline{uv}$, demonstrated in Fig. 3(d). Deviation of $\overline{vw}$ from the fully converged, null statistical profile reflects the turbulence in the sampled volume that occurs within the down-sampled temporal and spatial range. Turbulence statistics from the sampled data shown in Fig. 3 significantly deviate from the fully converged statistics of the DNS by design. It is of interest in the following analysis to determine whether the proposed dynamical systems can predict turbulence statistics accurately with down-sampled data.

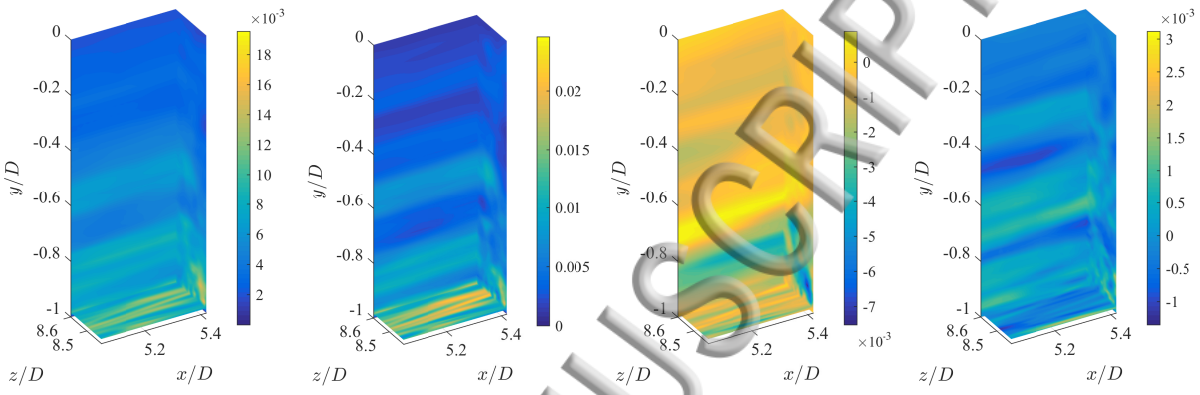

(a)k (b)$\overline{uu}$ (c)$\overline{uv}$ (d)$\overline{vw}$

FIG. 3. Turbulence kinetic energy and selected Reynolds stresses for sampled channel flow volume.

IV. POD

The POD is applied to the sample data where each snapshot is taken as a 3D field of fluctuating velocity. The cumulative summation of eigenvalues in Fig. 4 indicates the number of modes required to reach a desired threshold of the integrated kinetic energy. The distribution of eigenvalues normalized by their sum is shown in Fig. 4 (inset), which by definition demonstrate the distribution of turbulence kinetic energy per mode, normalized by the total turbulence kinetic energy. The low-order modes represent the largest portion of the integrated turbulence kinetic energy in the kernel according to the definition of the POD. The relatively flat portion of the spectrum in the inset figure corresponds to a large number of energy-containing modes. Beyond $n \sim 10^2$, the spectrum falls off quickly indicating a rapid decay in the energy carried by high-order modes.

In using volumetric data, the ability of the POD to quickly account for the full character of the flow is diminished and the resulting eigenvalue spectrum is accordingly flattened. The transverse and streamwise directions are characterized by periodic boundary conditions, and are considered to be homogeneous in fully converged statistics. Homogeneity in the kernel reduces the efficiency of the POD and causes modes to resemble those from a Fourier decomposition, retarding the convergence of the basis. Time resolution of the velocity snapshot sample is equal to the maximum resolution of the DNS data stored from the simulation, at every $t = 0.065$. At this resolution, velocity snapshots are not statistically independent, and correlation is expected between successive fields. The resulting POD coefficients are not considered uncorrelated in time as they are in other applications of the POD, but rather are each a time series.

According to the thresholds seen in Fig. 4, five modes are required to account for 50% of the integrated turbulence kinetic energy, 13 modes are required to reach 75%, and 28 modes are required to account for 90% of the energy in the kernel. The mode basis describes the turbulence; each mode is associated with spatially coherent turbulence structures in the input flow data. Individual structures illustrated by the POD modes are not discussed at length in the following development and are shown only to convey the fact that low-rank modes represent flow features in the center of the channel as well as in the near-wall region. Of the full basis, the only POD modes and coefficients specifically discussed in the following reduced

This manuscript was accepted by Phys. Fluids. Click here to see the version of record.

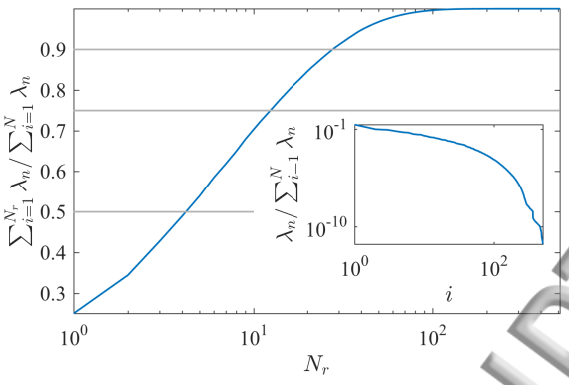

FIG. 4. POD eigenvalues showing the cumulative summation of energy and the normalized energy content by mode (inset). Thresholds accounting for 50%, 75%, and 90% of the turbulence kinetic energy shown in gray requiring $N_r = 5$, $N_r = 13$ and $N_r = 28$ modes, respectively

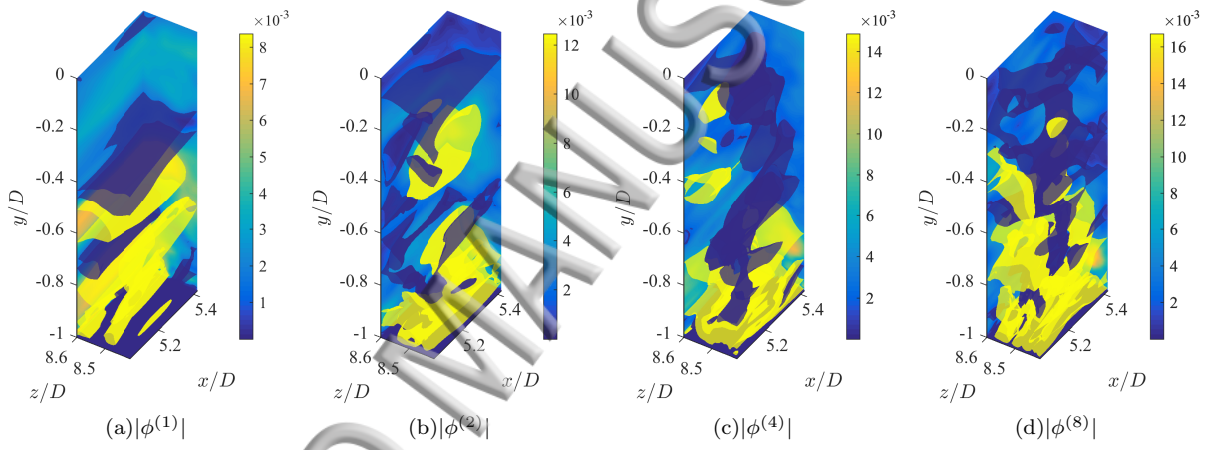

FIG. 5. Magnitude of selected POD modes used in reduced order models.

order model are modes 1, 2, 4, and 8. The magnitude of each selected mode is shown in Fig. 5. In each subfigure, from left are the vectorial magnitudes of modes in increasing order (decreasing energy), calculated as $|\phi^{(i)}| = \sqrt{\phi_x^{(i)2} + \phi_y^{(i)2} + \phi_z^{(i)2}}$. Color information is included for each mode to show that they have each been normalized, POD modes themselves are unitless and do not represent energy. It is only in linear combination with their respective dynamic coefficients that the POD modes are able to express the fluctuating velocity field.

Fig. 5 indicates that the near-wall behavior of the channel flow is present in many POD modes. The POD requires many modes to fully describe this behavior; large structures are seen in all three components of the POD modes away from the wall in the central region of the channel. The low-rank POD modes accounting for the majority of the integrated turbulence kinetic energy are used to formulate low-order dynamical systems in the following sections. The coefficients associated with modes including those shown in Fig. 5 are taken to express the dynamics of the turbulence and are discussed in greater detail below. An advantage to the POD is that modes are scaled based on energy content rather than time or length scales. This allows POD modes, in combination with their respective coefficients, to simultaneously contribute to the dynamics in the near-wall region and the center of the channel, provided that both regions are present in projections of the velocity field onto the POD subspace.

V. LOW ORDER DYNAMICAL SYSTEM

The dynamical system derived according to the formulation in section II B is expected to account for turbulence that includes fluctuations of spanwise velocity in the channel flow. Adding complexity, such as three-dimensional turbulence, to the reduced order models requires a large range of POD modes to accurately describe, but makes for a more relevant dynamical system. The capability of LODS to represent the full channel flow is tested according to the number of modes used to define the system. The modes analyzed in the following range between three modes (the minimum required to reconstruct 3D turbulence shown in Hamilton et al. [33] and 41 POD modes, corresponding to the 95% kinetic energy threshold from the cumulative summation of POD eigenvalues.

The traditional Galerkin projection is not discussed at length here as the resulting dynamical systems function best in cases where turbulence is relatively low unless auxiliary turbulence mechanisms are added for stability [10]. Galerkin-POD systems have already been investigated for a pipe flow in Aubry et al. [6] and a channel flow in Ilak and Rowley [38], although the Reynolds number is moderate in each case. In the current study, the centerline Reynolds number $Re_c \sim 2.3 \times 10^4$, an order of magnitude larger than the previous documented reduced order modeling techniques. The Galerkin projection for this flow would be of benefit for comparison to the current work, and may be a beneficial platform for testing current efforts in model balancing with non-linear eddy viscosity models.

Rather than projecting modes onto the governing equations and seeking ODEs for the coefficients, the low-order system pursued here follows the least-squares fit method of the time-varying coefficients directly. The dynamical system predicting the behavior of the mode coefficients is obtained from the derivatives of the coefficients from the POD. The least-squares type LODS requires simultaneous realizations of both a_i and da_i/dt. Data sampled from the channel flow DNS have sufficiently high temporal resolution to yield accurate estimates of the time derivatives of the POD mode coefficients. Corresponding with the 90% threshold, 28 POD modes are used to establish the LODS parameters seen in Fig. 6. The LODS of this rank (28 modes, 90% energy) is used in the recalibration discussed below. Although the parameters resulting from the least-squares fit shown in Fig. 6 do not arise from projection onto the governing equations, they are interpreted analogously where possible. The constant parameter D_i is quite small compared to the others employed in the current analysis. One interpretation of the constant parameter from the perspective of dynamical modeling is as long-term growth or instability of each respective POD mode; that these parameters are small but non-zero implies that they are subject to amplification or decay and may ultimately lead to long term instability if higher-order relationships are not taken into account. Transient or spatially developing turbulence could be reflected by mode amplitudes that are not zero-centered, which the constant parameter would attempt to correct. In a traditional Galerkin projection, the linear parameter L_{ij} arises from the viscous term in the Navier-Stokes equations. The contribution to the viscous dissipation is largely accounted for by the smallest scales of turbulence, not accounted for in the truncated mode basis. L_{ij} is the largest in magnitude of the fit parameters indicating a strong linear interaction between modes. The linear parameter is anti-symmetric about the diagonal $i = j$, and is of greatest magnitude in the off diagonals where $i = j \pm 1$. This is taken to indicate that the linear interaction is strongest in modes of similar rank.

Through analogy to the Galerkin-POD procedure, the quadratic parameters Q_{ijk} are taken to represent the combined contributions of convective and pressure terms. Effects of the mean flow field and the fluctuating pressure reflected in the LODS though the turbulent dynamics, although they do not appear as variables as far as of the polynomial parameters. In the interpretation of the Galerkin projection, fixing $j = 0$ or $k = 0$ is typically associated with convection. In the LODS developed here, the mean flow field is omitted and the POD basis does not include a zeroth index. The mean flow *is* implicitly included in the model through the velocity snapshots although it is not considered as a variable in the dynamical system. Permuting the indices j and k in the quadratic term yields identical values; the interactions expressed by Q_{ijk} are of mode i with a combination of j and k.

LODS parameters couple the mode coefficients $\hat{a}_i$ in the system of ODEs to be solved as in equation (5). The degree to which a mode is coupled to any others is shown as the relative magnitudes of each parameter. Extreme values imply strong correlation or anti-correlation in the dynamic evolution of the modes. Small values of the parameters are taken to indicate that a combination of the modes in question is negligible in the evolution of the system. The least-squares fit from equation (7) matches da_i/dt calculated from the time series of POD mode coefficients to one solved in the ODEs $d\hat{a}_i/dt$, shown in Fig. 7(a). The figure shows the polynomial fit of the LODS to the time derivatives of the POD coefficients in the sample space (black lines). Fits shown in the Fig. 7 use $N_r = 5$ (dashed gray lines), $N_r = 13$ (solid gray lines), $N_r = 28$

This manuscript was accepted by Phys. Fluids. Click here to see the version of record.

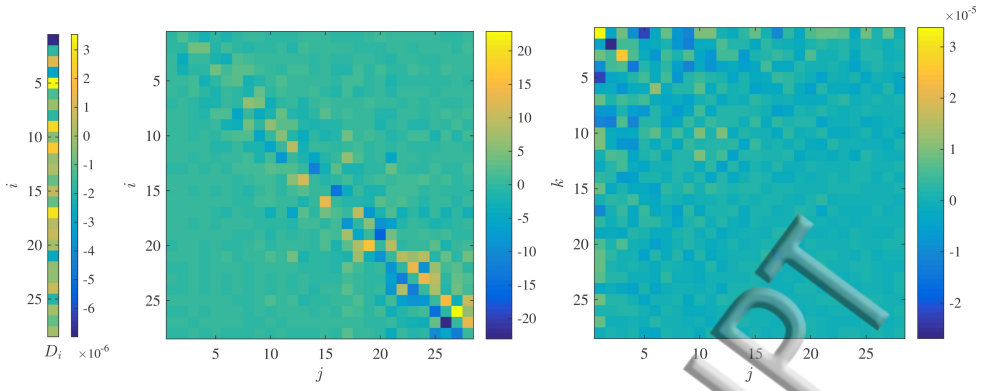

(a)D_i (b)L_{ij} (c)Q_{ij1}

FIG. 6. Constant 6(a), linear 6(b), and quadratic 6(c) parameters from least-squares fit of $d\hat{a}_i/dt$ using 28 modes. For the quadratic term shown, the index $k = 1$ is fixed and other components are omitted. Cubic term is not shown for brevity.

(dotted gray lines), $N_r = 41$ (dash-dot gray) modes accounting for 50%, 75%, 90%, and 95% of the energy of the input data, respectively. Trends of the fit of $d\hat{a}_i/dt$ indicate that truncating the modal basis acts as a low-pass filter on da_i/dt. Major features of the time derivatives are well-represented with few modes but higher frequency dynamics of a_i are missed in the LODS of low rank.

Solving the ODEs results in predictions of coefficients $\hat{a}_i$ shown in Fig. 7(b). As with their time derivatives, the POD coefficients are shown in black lines and those resulting from reduced order model are shown in gray. Initial conditions are required for solutions, taken here as the first value of each coefficient from the POD, corresponding to $t = 0$ from the channel flow DNS. The choice of initial conditions is arbitrary and the resulting approximations $\hat{a}_i$ evolve distinctly for each choice, although choosing $a_0 = a_i(t = 0)$ is convenient in that the coefficients take a known trajectory from this point to which the model may be compared. Sensitivity of the solution to initial conditions is exploited below to recalibrate the LODS and extend the predictions far past the input time.

Deviation from the time derivatives of the POD coefficients and their respective least squares fits (da_i/dt and $d\hat{a}_i/dt$) propagate through the solution of the ODEs seen clearly in the difference between a_i and $\hat{a}_i$ in Fig. 7(b). The fit between the POD coefficients and their respective predictions by the LODS are best for low mode number n and for high LODS rank N_r. Error propagation through the solution of the ODEs is most notable in the highest modes used in the LODS. Deviation from the expected trajectory is seen clearly for modes $n = 4$ and $n = 8$ for low-ranking LODS, bottom of the figure. When using 13 modes (accounting for 75% of the input energy), the coefficient $\hat{a}_8$ is nearly periodic and does not match the POD coefficients accurately. Error propagation beyond the input time of the sampled DNS grows quickly to the point where modeled coefficients $\hat{a}_i$ eventually diverge and numerical solution is no longer possible. The ability to predict outside of the input time depends on the number of modes used to formulate the LODS and the error tolerance in the numerical solution of equation (5).

Expanding the basis to include $N_r = 28$ adds a greater number of mode interactions to the LODS and is able to account for a broader range of dynamics. The time derivatives shown in Fig. 7(a) demonstrate a tighter fit than in the 5-mode LODS, as expected. Error is reduced by allowing a greater range of mode coupling through the fit parameters. In the 14-mode LODS, significant deviations between da_i/dt and $d\hat{a}_i/dt$ are not seen until $n = 16$. Increasing the mode basis used in the LODS and decreasing the error propagated through the ordinary differential equations naturally increases the ability of the LODS to predict the mode coefficients, shown in Fig. 7(b). As with the 5-mode LODS, error that propagates through the solution of the coupled ODEs is seen in the predicted coefficients $\hat{a}_i$. For consistency of comparison, the LODS is restricted to making predictions within the timespan of the sampled velocity snapshots.

To quantify the goodness of fit between the POD and LODS coefficients, the normalized RMS error is calculated as,

$$\mathrm{NRMSE}(\hat{g}) = \frac{\sqrt{\overline{(g - \hat{g})^2}}}{\max(g) - \min(g)}, \tag{8}$$

This manuscript was accepted by Phys. Fluids. Click here to see the version of record.

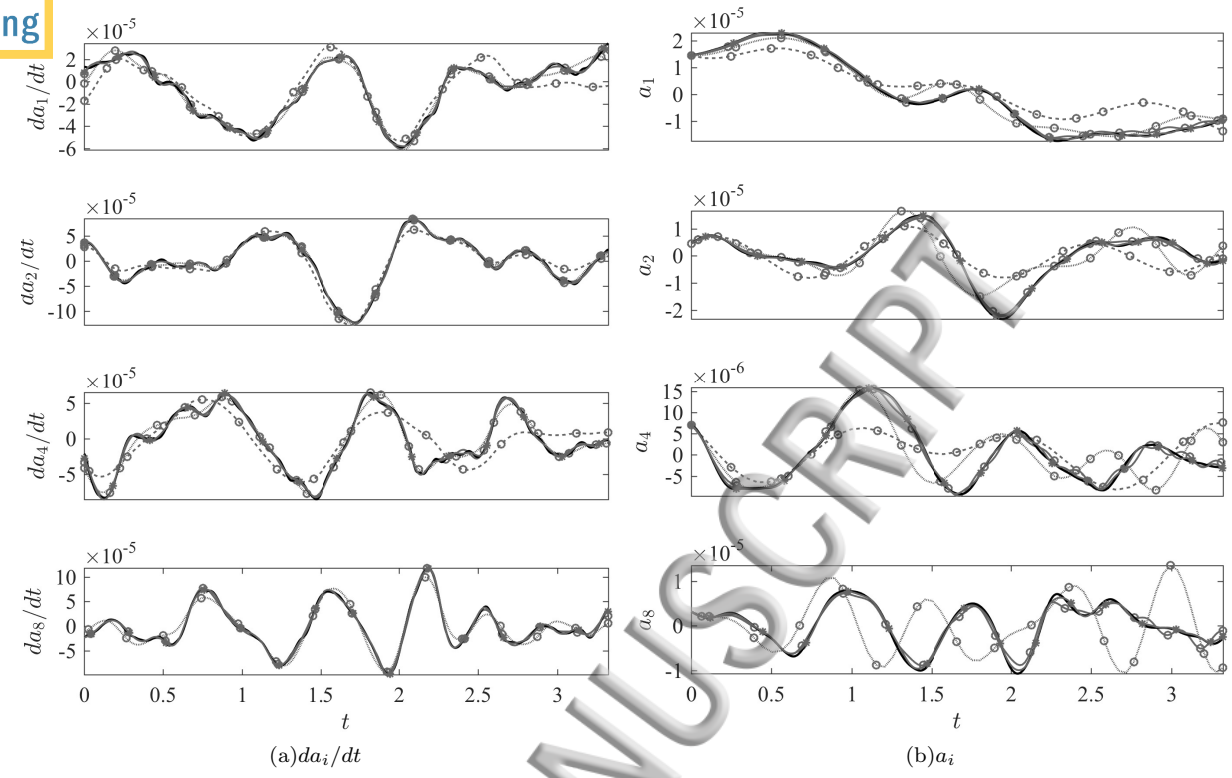

FIG. 7. Time derivatives of POD mode coefficients (black) and their respective LODS approximations in gray with symbols. Increasing the rank of the LODS leads to better fit between coefficients 7(b) and derivatives 7(a). For each subfigure, $N_r = 5$ dashed gray lines, $N_r = 13$ solid gray lines, $N_r = 28$ dotted gray lines, $N_r = 41$ dash-dot gray lines.

where g is a reference quantity (e.g. coefficients from the POD), $\hat{g}$ is the quantity derived via LODS, and the root-mean-square error is normalized by the span of the reference quantity.

For the LODS, error is calculated between the coefficients a_i and $\hat{a}_i$. Fig. 8 shows the normalized RMS error of the selected modes discussed above as a function of the LODS rank. Coefficients evolving from the LODS have a resolution in time that is a function of the numerical tolerance of the solver. In order to make difference calculations, the predicted coefficients $\hat{a}_i(\hat{t})$ are interpolated to the original time input t. Interpolation of the derivatives is not necessary as they are calculated to fit the input time by definition. Reflecting the trends seen in Figures 7(a) and 7(b), the error associated with the derivative of any particular mode coefficient decreases as a function of the number of modes used in the truncated POD basis N_r. It is not always the case, however, that the normalized RMS difference increases with n for a fixed basis N_r; there many cases in which a higher ranking modes exhibit less error than a low rank mode within a given basis.

The normalized RMS error between mode coefficients and their LODS predictions is not as well-behaved as the error for the derivatives. In a general sense, NRMSE($\hat{a}_i$) decreases as a function of the rank of the LODS, indeed the limit of the RMS error must be zero as $N_r \to N$, but the decrease in error does not appear to be monotonic. For example, the normalized RMS error between a_1 and $\hat{a}_1$ for $N_r = 15$ is much larger than for LODS of lower rank. These trends reflect dynamics added to the system through the mode interactions described by the LODS parameters. However, added mode interactions do not necessarily follow predictable and regular increase the performance of the dynamical system, and certain mode interactions may lead to a *decrease* in LODS accuracy. RMS errors for $\hat{a}_i$ and $d\hat{a}_i/dt$ are shown in Figures 8(b) and 8(a) for selected mode coefficients considering LODS up to rank $N_r = 41$. The normalized RMS error for $d\hat{a}_i/dt$ is smoother overall than that of $\hat{a}_i$. Interestingly, the error associated with $d\hat{a}_2/dt$ is less than that of mode 1 for all of the LODS tested, regardless of rank. Mode 1 characterizes the turbulence structures most important to the dynamics of the input. Accordingly, it interacts strongly with other modes and its time-evolution converges toward the expected value slowly.

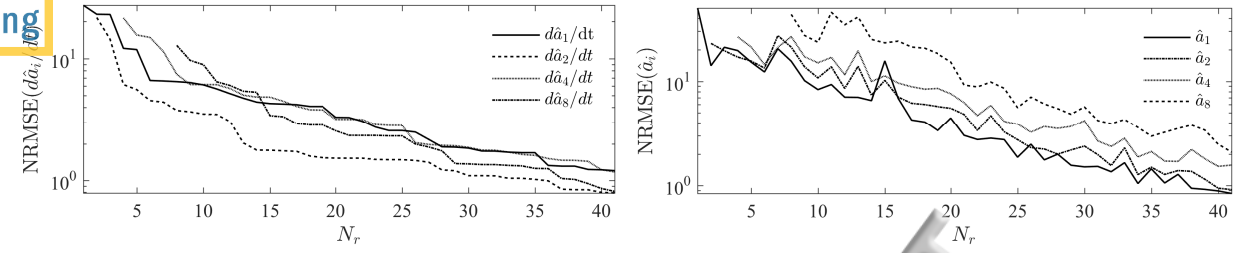

(a)Normalized RMS error of coefficients derivatives for modes 1, 2, 4, and 8 according to rank of the LODS.

(b)Normalized RMS error of coefficients for modes 1, 2, 4, and 8 according to rank of the LODS.

FIG. 8. Error associated with selected mode coefficients according to total number of modes composing the LODS.

VI. PERIODIC LODS RECALIBRATION

Numerical solutions presented above propagate error through $\hat{a}_i$ that compiles and causes the system to grow unstable and diverge at long solution times. The dynamics determined by the parameters D_i, L_{ij}, Q_{ijk}, and C_{ijkl}, specify mode interactions; the trajectory of the system also requires initial conditions, above taken as $a_i(t=0)$. Using different initial conditions produces distinct coefficient evolutions that obey the dynamics specified by the LODS parameters. The sensitivity of the LODS to supplied initial conditions is used as a means to periodically recalibrate the solution, resulting in a more robust system capable of making predictions at much longer solution times.

Recalibration is undertaken by matching the vector of LODS coefficients at the end of the integration time $\hat{a}_i(t=t_f)$ to the known history of the POD coefficients. The time to which the vector of coefficients is matched is determined by minimizing the RMS difference between $\hat{a}_i$ and a_i. The time index of the matched data is denoted with the subscript m and is referred to as the 'matching time'. New initial conditions are provided using the POD coefficients at the matching time,

$$a_i(t_m) \ni \min \sqrt{\frac{1}{N_r}\sum_{i=1}^{N_r}(a_i(t_m)-\hat{a}_i(t_f))^2}, \qquad 0 \le t_m \le t_f. \tag{9}$$

With refreshed initial conditions, a new solution to equation (5) is calculated and concatenated with the previous solution. In the mode coefficient matching process, the matched coefficients a_i are piecewise continuous across the recalibration and remain bounded in the ranges resulting from the POD. To prevent the LODS from falling into a closed orbit, the time span of each integration is assigned randomly up to the length of the original input signals, $t = 3.32$. Recalibration of the LODS limits the error propagation in the coefficients at the cost of introducing discontinuities in $\hat{a}_i$. Sharp discontinuities in the predicted histories of the mode coefficients are limited by adding further constraints to the recalibration process. A short region is defined between periods of recalibration in which the solution which $\hat{a}_i$ are interpolated between t_f and t_m. At both ends of the interpolated region, the derivatives $d\hat{a}_i/dt$ are matched and the predicted coefficients are smoothed to reduce potential discontinuities introduced to velocity reconstructions.

The sensitivity of the LODS to initial conditions is beneficial in that it implies a ready supply of starting points are available within the known trajectories of a_i. However, the number of possible initial conditions is limited to the number of snapshots in the input data. Stated otherwise, the finite record of snapshots is represented as a finite number of linear combinations of modes and coefficients, in this case $N = 512$, and can thus predict a finite number of coefficient trajectories. This constrain is relaxed by guiding the vector of coefficients $\hat{a}_i(t_f)$ toward their matched values, rather than replacing them directly with $a_i(t_m)$. The effect is to find a vector of coefficients that is intermediate to both the above vectors,

$$a_{0,\mathrm{new}} = (\alpha)a_i(t_m) + (1-\alpha)\hat{a}_i(t_f). \tag{10}$$

The weighting coefficient α determines the balance between a known vector of coefficients from the POD history $a_i(t_m)$ and the final predicted value from the LODS $\hat{a}_i(t_f)$. The effect of guiding the coefficients from the LODS to new values makes a more complete range of coefficients available as initial conditions, rather than restricting them to the 512 known combinations from the POD history. In the following demonstration

of LODS recalibration, the weighting coefficient is assigned to $\alpha = 0.5$ making the new initial conditions exactly half way between the final predicted coefficient vector and its closest match from the POD history.

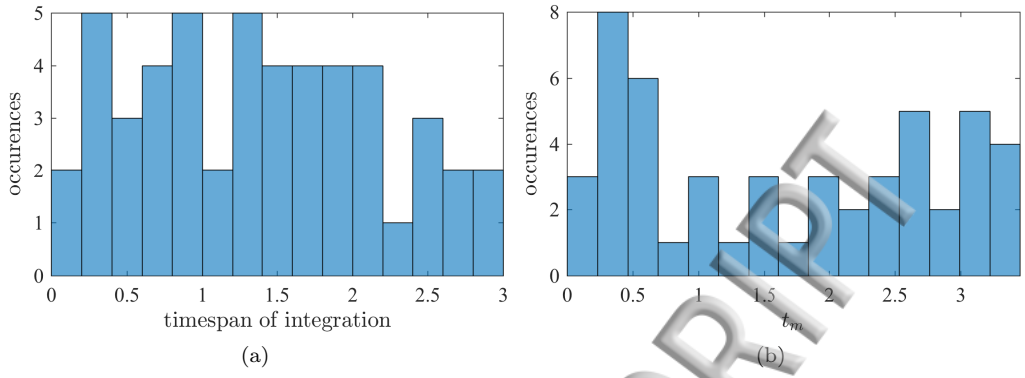

FIG. 9. Histograms depicting 9(a) the timespan of the new ODE solution and 9(b) the matching time for new initial conditions in the periodic recalibration process.

The length of integration times is assigned randomly between the range $0 \leq t \leq 3.32$. With sufficient instances of recalibration, the histogram of timespans tends toward a flat distribution. Fig. 9(a) shows the integration timespans of a low-order dynamical system undergoing 50 periods of recalibration. The associated distribution of matching times t_m after the same 50 instances of recalibration is shown in Fig. 9(b). While the distribution of timespans should be flat by definition, the distribution of t_m is not similarly constrained. Coefficients from the LODS $\hat{a}_i$ are compared to those from the POD record a_i in Fig. 10. The figure indicates that the modeled mode coefficients $\hat{a}_i$ remain bounded in the neighborhood of a_i. The recalibration process allows the coefficients to take on values outside of their known histories from the POD. The dynamics are limited to making predictions determined by the LODS parameters, but the original POD coefficients account for only 512 states, corresponding to the 512 snapshots from the sampled data. By allowing the vector of coefficients to take on new values, the predicted coefficients fill the vector space defined by the truncated POD basis.

In extending the time series of the modeled coefficients, additional features of their time evolution become evident. Each of the selected modes in Fig. 10 shows some periodicity that is determined by the dynamics of the input. Here the LODS with 50 recalibrations spans up to approximately $t = 95$, more than 3 times as long as the full DNS and nearly 30 times the sampled data. The modeled coefficient for mode 1 shows large, low-frequency features. In any application of the POD, the first modes are associated with energetic turbulence structures. The predicted coefficient $\hat{a}_1$ has a range that is approximately 50% larger than its equivalent in the range of the sampled data, but does not grow unstable with the recalibration scheme. Because only a limited range of DNS data was sampled, it is reasonable to expect that the coefficients produced by the POD might not represent the full range required to reconstruct every snapshot in the simulation. During recalibration, the modeled coefficients take on combinations of values not explicitly contained in the set of a_i, effectively increasing the density of the coefficients within a similar space. The other coefficients shown in Fig. 10 instead take on smaller ranges outside of the input time, and appear more noisy. Despite the smoothing employed at the boundaries of each recalibration, noise is introduced to the system whenever the initial conditions are reset.

Ultimately, it is of interest to compare the performance of the LODS to the POD and the statistics of the sampled data in terms of turbulence. The fluctuating velocity field was reconstructed using the POD coefficients according to equation 1, and subsequently used to calculate the modeled Reynolds stress tensor $\overline{\hat{u}_i \hat{u}_j}$. Reconstructing the turbulence field with a truncated POD basis amounts to applying a non-linear low-pass filter to the input data according to energy; any representation of the turbulence field produced by a truncated POD basis must necessarily contain or describe less turbulent kinetic energy than the full field description in a global sense. However, shear terms may be *over* represented by a truncated basis. When this is the case, higher-order modes leak energy from the shear terms, although they make a positive global contribution to the TKE. Fig. 11 compares the streamwise normal stress calculated from the input snapshot basis, the reduced order description from the truncated POD basis, and the periodically recalibrated LODS, respectively from left. Only the streamwise normal stress is visualized as it is the dominant contributor to

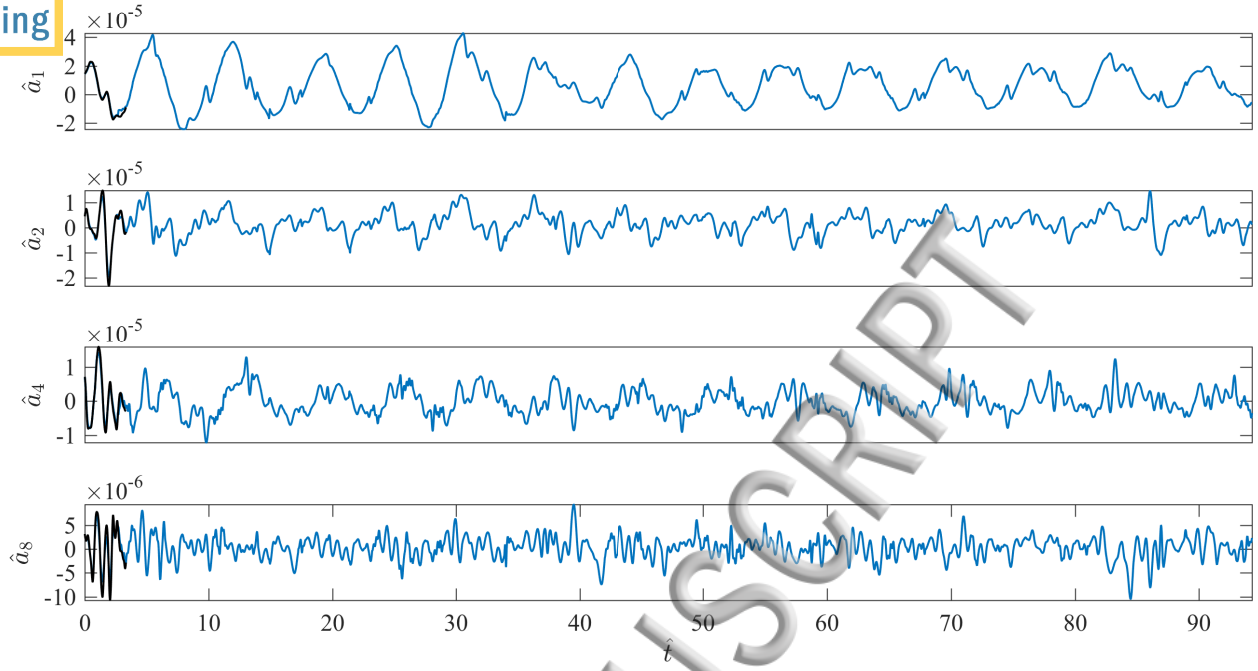

FIG. 10. POD mode coefficients (black) and their respective LODS approximations (blue) calculated from the time derivatives shown in Fig. 7(a) after 50 periods of recalibration.

the turbulence kinetic energy. As anticipated, the POD estimate of $\overline{uu}$, Fig. 11(b), picks out the large scale, energetic features of the statistically derived Reynolds stress shown in Fig. 11(a). Large structures below $y/H = -0.5$ are captured successfully by the POD, including features very near the wall. Features captured by the LODS in Fig. 11(c) are similar to the POD estimates. Differences between the POD and LODS estimates are seen most clearly in the near-wall region. The LODS exaggerates the effects of POD filtering; regions of low stress appear muted, and regions of high stress (near the wall and around $y/H = -0.5$) are amplified compared to the POD reconstruction.

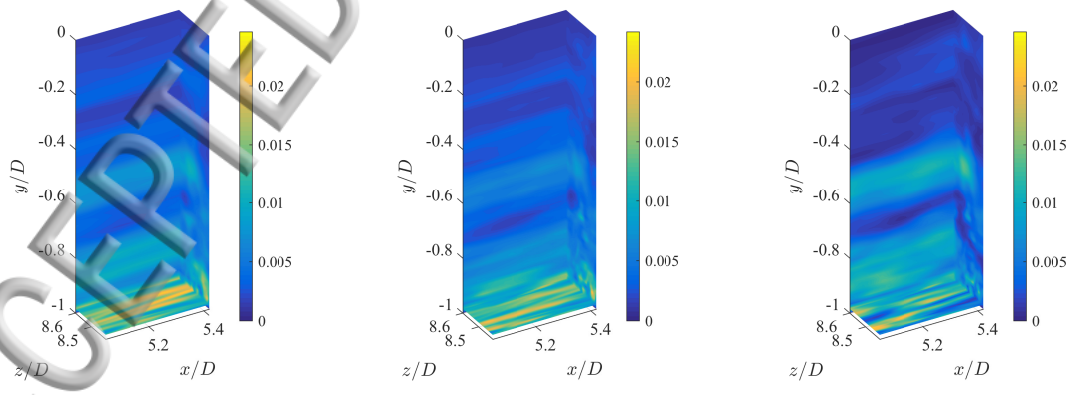

(a)$\overline{uu}$ (b)POD estimate of $\overline{uu}$. (c)LODS estimate of $\overline{uu}$.

FIG. 11. Comparison of streamwise normal Reynolds stress from sample statistics, POD reconstruction, and LODS estimate, from left.

Comparing the streamwise/wall-normal Reynolds shear stress $\overline{uv}$ as in Fig. 12, it is evident that the LODS makes predictions not seen by the POD estimate. Fig. 12(c) predicts a second structure of high magnitude in the center of the channel. This structure is not present in either the POD or the sampled statistics, showing that the model is predicting outside of the input dynamics. Both the POD and the LODS exaggerate regions

where $\overline{uv} \geq 0$ for $y/H \geq -0.6$; although neither the POD nor the LODS have any difficulty reproducing the character of the shear stress. The superposition and interaction of a large basis of modes is necessary to converge toward null values of the stresses far from the wall.

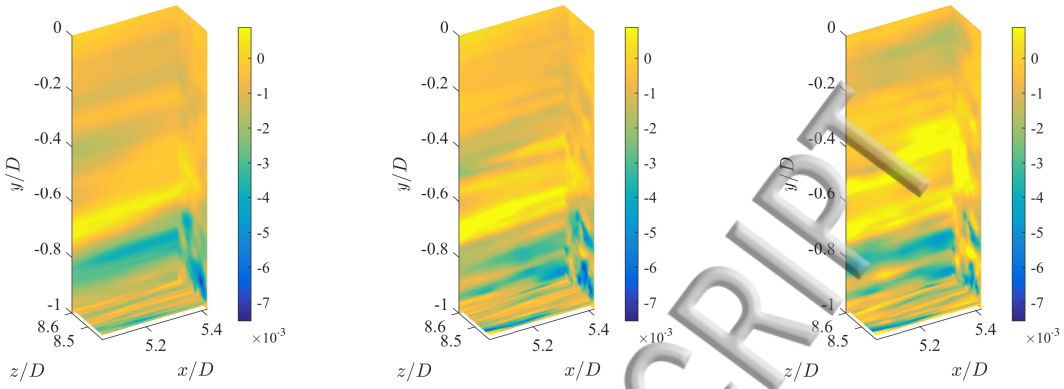

(a)$\overline{uv}$ (b)POD estimate of $\overline{uv}$. (c)LODS estimate of $\overline{uv}$.

FIG. 12. Comparison of streamwise/wall-normal Reynolds shear stress from sample statistics, POD reconstruction, and LODS estimate, from left.

To benchmark the performance of the LODS, profiles of spatially averaged quantities are compared in Fig. 13. In each subfigure, a single component of the Reynolds stress tensor is averaged in the streamwise and spanwise directions, denoted with angle brackets $\langle\cdot\rangle$. Subfigures compare the spatially averaged turbulence stresses for the full channel flow DNS as a dashed black line, reproduced from Graham et al. [32], with the profiles from the sampled statistics (gray lines), the truncated POD basis (blue), and the LODS (orange). From the figure, it is clear that the LODS makes estimations of the Reynolds stresses in the channel that are at least as accurate as those derived from the truncated POD basis. In certain areas of the flow, the LODS makes estimations of the turbulence stresses that are quite similar to those of the full DNS. The flow description of the LODS has a longer time record due to the periodic recalibration algorithm and is able to fill out the state space of the coefficients. Letting the coefficients take on values other than those provided in the POD history effectively accounts for snapshots that obey the dynamics of the channel flow, but are not contained in the original sample. The relationships defined by the LODS parameters dictate the limits of the system dynamics, and allow for more possible states than the training data.

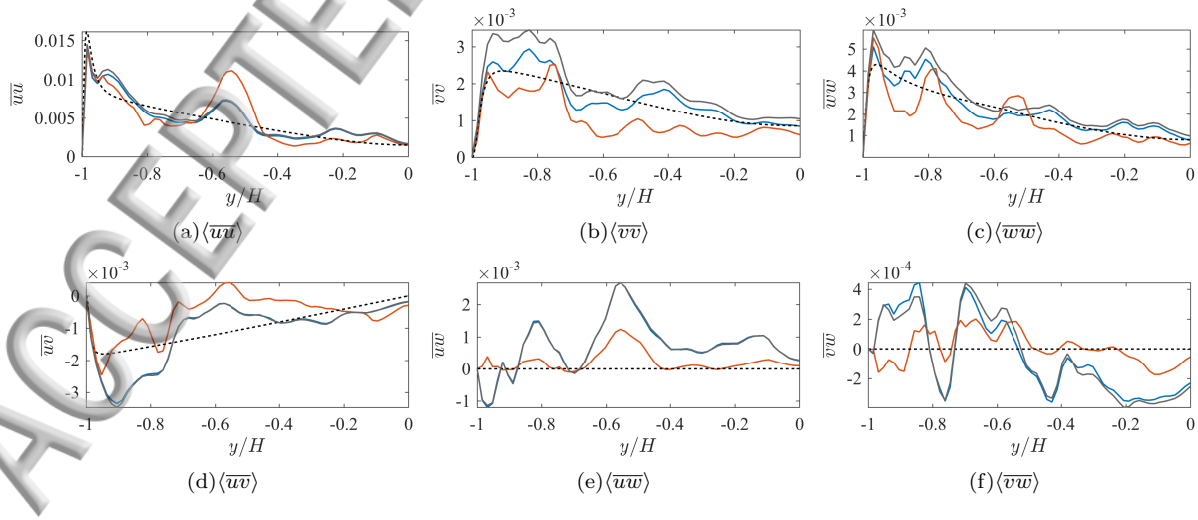

(a)$\langle\overline{uu}\rangle$ (b)$\langle\overline{vv}\rangle$ (c)$\langle\overline{ww}\rangle$

(d)$\langle\overline{uv}\rangle$ (e)$\langle\overline{uw}\rangle$ (f)$\langle\overline{vw}\rangle$

FIG. 13. Spatially averaged profiles of Reynolds stresses comparing statistics of sampled data (black), POD reconstructions (blue), and LODS with periodic recalibration (orange) to the spatially averaged profile from the full DNS (black,dashed).

Profiles of the spatially averaged Reynolds normal stresses are easily compared in Figure 13. The LODS makes approximations of the streamwise normal stress that are within 8% of the full DNS statistics except between $-0.65 \leq y/H \leq -0.45$. In this region, the LODS exaggerates a peak in the Reynolds stress present in the sampled data and subsequently in the POD. The wall-normal Reynolds stress in Fig. 13(b) is a close fit in the near wall region and in the center of the channel. Between $-0.9 \leq y/H \leq -0.1$, the LODS underestimates $\langle\overline{vv}\rangle$. The spanwise Reynolds normal stress meanders around the profile for the full DNS between $-0.9 \leq y/H \leq -0.25$. It is hypothesized that with a longer simulation time or greater flexibility in the recalibration process, $\langle\overline{ww}\rangle$ may converge toward the DNS profile more closely. Fig. 13 demonstrates that the LODS is easily distinguished in terms of the turbulence shear stresses. For example, the LODS profile of $\langle\overline{uv}\rangle$ makes a better estimate near the wall than the sampled statistics or the POD approximation. Spatially averaged shear stresses $\langle\overline{uw}\rangle$ and $\langle\overline{vw}\rangle$ tend toward zero with perfect statistical convergence and are typically excluded in channel flow discussions as spanwise fluctuations are less important than those in the streamwise and wall-normal directions. The dashed lines in Figures 13(e) and 13(f) are set to *identically* zero, and do not come from the DNS documentation. For these shear stresses, the profiles of the LODS are much closer to the expected values than the other approximations.

TABLE II. Normalized RMS error (%) between the DNS turbulence field and approximations from the sampled data, the POD description, and the LODS with periodic recalibration. For the shear stresses $\overline{uw}$ and $\overline{vw}$, errors are normalized by the span of each respective approximation, as the range for the DNS is identically zero.

	$\overline{uu}$	$\overline{vv}$	$\overline{ww}$	$\overline{uv}$	$\overline{uw}$	$\overline{vw}$
Sample	8.03	21.78	16.33	40.93	0.28	0.32
POD	7.79	23.73	18.65	40.81	0.28	0.32
LODS	13.61	26.41	21.1	36.98	0.30	0.28

Normalized RMS errors according to equation (8) are calculated for the spatially averaged profiles shown in Fig. 13, detailed in Table II. Quantifying the deviation between the spatially averaged profiles of $\overline{u_i u_j}$ and the estimates from the reduced order descriptions indicates that the LODS error across the channel half-height is slightly greater that for the POD. From Fig. 13 it is clear that errors arise from localized events. The greatest increase in rms error is seen for $\overline{uu}$, approximately 5%. Error shown for the shear stresses $\overline{uw}$ and $\overline{vw}$ are very similar to those of the POD and the sample, although the figure clearly demonstrates that the LODS makes a better estimate. For these shear stresses, the DNS profiles are identically zero and the normalization used in equation (8) is inappropriate; for $\overline{uw}$ and $\overline{vw}$, the RMS error is normalized by the span of the estimator rather than the span of the DNS profile, leading to the similar values in the table.

VII. CONCLUSIONS

Low order dynamical systems are formulated for the fully-developed turbulent channel flow DNS hosted at Johns Hopkins University. The dynamical system is derived by seeking a set of parameters that quantify mode interaction and result in a system of coupled ODEs through a least-squares polynomial fit. The LODS demonstrated in this study combines the time-dependent POD mode coefficients directly in formulating a dynamical system, in contrast with the Galerkin projection, which instead seeks a dynamical system through the inner product of the Navier-Stokes equations with spatially coherent proper orthogonal modes. Parameters resulting from the LODS are analogous to those from the Galerkin projection; in addition to the linear and quadratic terms in the Galerkin system, there are constant and cubic terms, which add both complexity and stability to the dynamics.

The LODS composed here for the turbulent channel flow does not arise from a mathematical projection onto the governing behavior law of the flow. While this may appear to limit the physical significance of the dynamical system, it also adds generality to the method. In removing the physical meaning associated with each set of parameters, they become more flexible, in that they may take on a range of values that might appear inconsistent with the behavior laws governing the flow, but are within the limits for dynamics defined by the input data. At the same time, extending an analogy to the linear and quadratic parameters provides an estimate of the influence of viscous or convective terms in the LODS. An additional benefit in the current definition of the reduced order model is that it derives all flow parameters implicitly from the input data, whereas the Galerkin-POD procedure requires that parameters like eddy viscosities be supplied by the user.

A difference between the LODS and DNS statistics is expected; spatially averaged profiles of the Reynolds stresses demonstrate that the low-order dynamical system can reproduce the turbulence within 5% of the statistical error of the sampled data. The dynamics included in the system are defined by the parameters that quantify mode interaction, and ultimately reflect the data included in the sampled basis of velocity snapshots. The sample used to compose the LODS represents a small slice of the full simulation; the complete set of dynamics and turbulence was not included in the kernel of the POD and cannot be fully reproduced by the LODS.

It is of interest in reduced order modeling for any application to determine to what extent a system may account for dynamics beyond the training data. The POD algorithm provides a set of modes that describe spatially coherent components of the input. By increasing the dynamics accounted for in the kernel of the POD, the reduced order model above will be better equipped to match statistics drawn from the full simulation. A limitation to the LODS developed here is the need for simultaneous realizations of both the mode coefficients and their respective time derivatives, which are difficult to achieve for many practical applications. High-fidelity numerical simulations or time-resolved PIV and dual-time PIV measurements have been used in the past [21, 27] to accurately develop time derivatives of the POD mode coefficients.

The low-dimensional model explored here is capable of predicting velocity snapshots that are not included in the input data or the range of the dynamics from the POD mode coefficients. Using a larger set of sample data will produce POD modes that are statistically more converged, and will certainly lead to better approximation of the full DNS statistics. A thorough analysis of the system response to perturbations and input functions would advance the control capabilities of low-dimensional models like those composed here. Correlating an upstream signal with the POD coefficients would provide a more intuitive recalibration method, leading to accurate reflections of inflow disturbances. Control models of these sorts would be attractive for a variety of aerodynamics and flow control applications.

ACKNOWLEDGMENTS

The authors would like to acknowledge the U.S. National Science Foundation for supporting the above work (Grant Nos. NSF-ECCS-1032647 and NSF-CBET-1034581). In addition, Hamilton is grateful for support from National Science Foundation IGERT Grant No. 0966376. Work by M. Tutkun has been partially financed by the research project DOMT, funded by the Research Council of Norway with project number 231491 under the FRINATEK program.

[1] K. Hasselmann, Journal of Geophysical Research: Atmospheres (1984–2012) 93 (1988) 11015–11021.
[2] D. Rempfer, Theoretical and Computational Fluid Dynamics 14 (2000) 75–88.
[3] J. L. Lumley, Atmospheric turbulence and radio wave propagation (1967) 166–178.
[4] L. Sirovich, Quarterly of applied mathematics 45 (1987) 561–571.
[5] B. R. Noack, K. Afanasiev, M. Morzynski, G. Tadmor, F. Thiele, Journal of Fluid Mechanics 497 (2003) 335–363.
[6] N. Aubry, P. Holmes, J. L. Lumley, E. Stone, Journal of Fluid Mechanics 192 (1988) 115–173.
[7] C. Braud, D. Heitz, G. Arroyo, L. Perret, J. Delville, J.-P. Bonnet, International journal of heat and fluid flow 25 (2004) 351–363.
[8] G. Tadmor, O. Lehmann, B. R. Noack, L. Cordier, J. Delville, J.-P. Bonnet, M. Morzyński, Philosophical Transactions of the Royal Society of London A: Mathematical, Physical and Engineering Sciences 369 (2011) 1513–1524.
[9] C. W. Rowley, T. Colonius, R. M. Murray, Physica D: Nonlinear Phenomena 189 (2004) 115–129.
[10] J. Östh, B. R. Noack, S. Krajnovic, D. Barros, J. Borée, Journal of Fluid Mechanics 747 (2014) 518.
[11] M. Pastoor, L. Henning, B. R. Noack, R. King, G. Tadmor, Journal of fluid mechanics 608 (2008) 161–196.
[12] C. W. Rowley, International Journal of Bifurcation and Chaos 15 (2005) 997–1013.
[13] O. Lehmann, M. Luchtenburg, B. R. Noack, R. King, M. Morzynski, G. Tadmor, in: Decision and Control, 2005 and 2005 European Control Conference. CDC-ECC'05. 44th IEEE Conference on, IEEE, pp. 500–505.
[14] B. R. Noack, P. Papas, P. A. Monkewitz, Journal of Fluid Mechanics 523 (2005) 339–365.
[15] M.-L. Rapún, J. M. Vega, Journal of Computational Physics 229 (2010) 3046–3063.
[16] B. Podvin, Physics of Fluids (1994-present) 21 (2009) 015111.
[17] B. R. Noack, M. Morzynski, G. Tadmor, Reduced-order modelling for flow control, volume 528, Springer Science & Business Media, 2011.

[18] J. Fike, Sandia National Laboratories Report, SAND (2013).
[19] J. Favier, L. Cordier, A. Kourta, A. Iollo, in: ASME 2006 2nd Joint US-European Fluids Engineering Summer Meeting Collocated With the 14th International Conference on Nuclear Engineering, American Society of Mechanical Engineers, pp. 743–748.
[20] S. Brunton, B. Noack, Applied Mechanics Reviews 67 (2015) 050801.
[21] L. Perret, E. Collin, J. Delville, Journal of Turbulence (2006) N17.
[22] W. Polifke, Annals of Nuclear Energy 67 (2014) 109–128.
[23] S. Sirisup, G. E. Karniadakis, D. Xiu, I. G. Kevrekidis, Journal of Computational Physics 207 (2005) 568–587.
[24] R. Romijn, L. Özkan, S. Weiland, J. Ludlage, W. Marquardt, Journal of Process Control 18 (2008) 906–914.
[25] L. Cordier, B. R. Noack, G. Tissot, G. Lehnasch, J. Delville, M. Balajewicz, G. Daviller, R. K. Niven, Experiments in fluids 54 (2013) 1580.
[26] M. Couplet, C. Basdevant, P. Sagaut, Journal of Computational Physics 207 (2005) 192 – 220.
[27] J. D'adamo, N. Papadakis, E. Memin, G. Artana, Journal of Turbulence (2007) N9.
[28] M. Bergmann, L. Cordier, Journal of Computational Physics 227 (2008) 7813–7840.
[29] L. Cordier, E. Majd, B. Abou, J. Favier, International Journal for Numerical Methods in Fluids 63 (2010) 269–296.
[30] I. Kalashnikova, S. Arunajatesan, M. F. Barone, B. G. van Bloemen Waanders, J. A. Fike, Sandia National Laboratories Report, SAND (2014).
[31] M. Benosman, J. Borggaard, B. Kramer, arXiv preprint arXiv:1604.04586 (2016).
[32] J. Graham, M. Lee, N. Malaya, R. Moser, G. Eyink, C. Meneveau, K. K. R. Burns, A. Szalay, Turbulent channel flow data set, Johns Hopkins University, 2013.
[33] N. Hamilton, M. Tutkun, R. B. Cal, Physical Review Fluids 2 (2017) 014601.
[34] Y. Li, E. Perlman, M. Wan, Y. Yang, C. Meneveau, R. Burns, S. Chen, A. Szalay, G. Eyink, Journal of Turbulence (2008) N31.
[35] E. Perlman, R. Burns, Y. Li, C. Meneveau, in: Proceedings of the 2007 ACM/IEEE conference on Supercomputing, ACM, p. 23.
[36] J. Kim, P. Moin, R. Moser, Journal of fluid mechanics 177 (1987) 133–166.
[37] M. Lee, N. Malaya, R. D. Moser, in: Proceedings of the International Conference on High Performance Computing, Networking, Storage and Analysis, ACM, p. 61.
[38] M. Ilak, C. W. Rowley, Physics of Fluids (1994-present) 20 (2008) 034103.

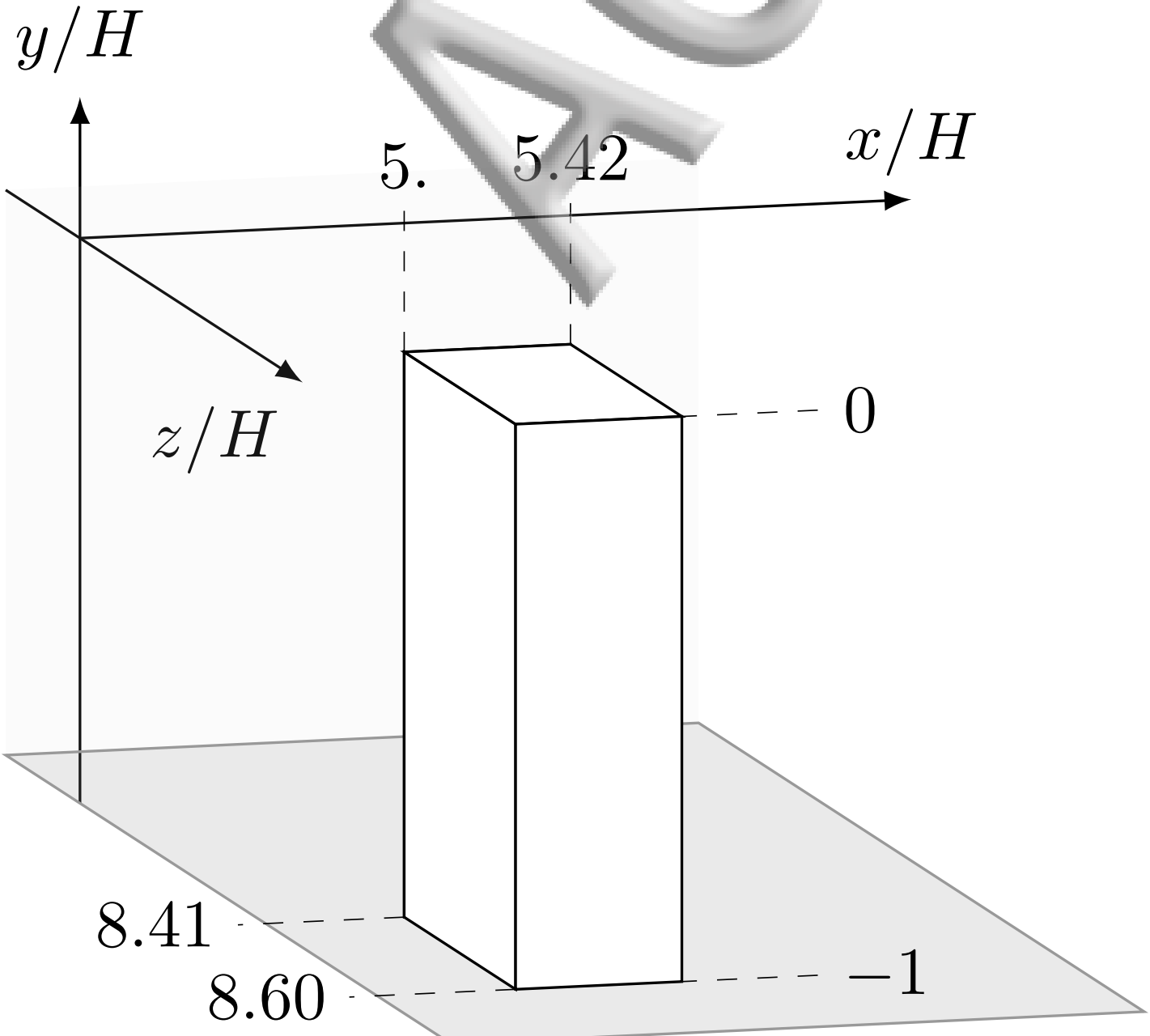
y/H
x/H
z/H
5.
5.42
0
8.41
8.60
-1

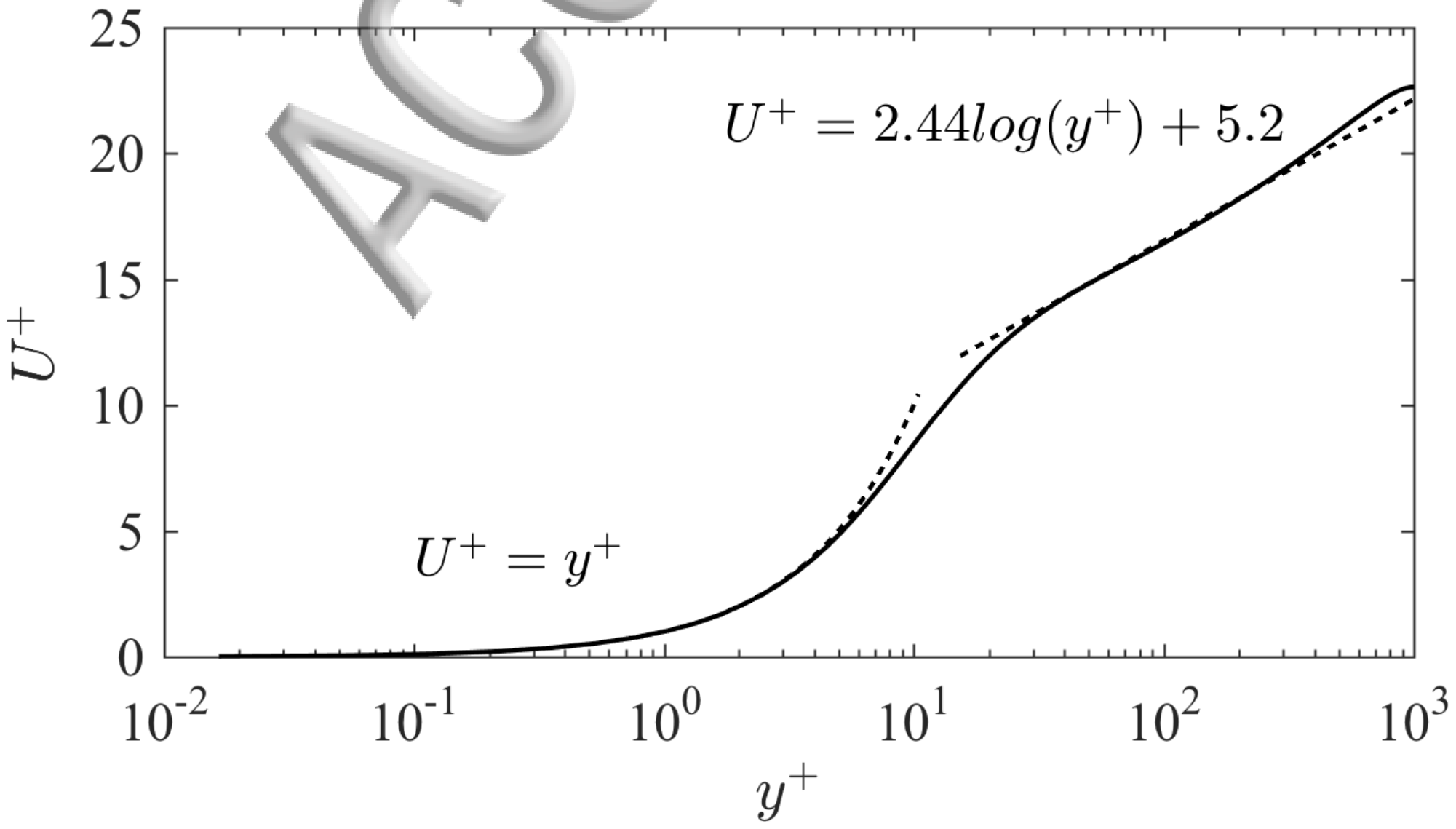
$U^+ = 2.44log(y^+) + 5.2$
$U^+ = y^+$
U^+
y^+
0
5
10
15
20
25
10^{-2}
10^{-1}
10^{0}
10^{1}
10^{2}
10^{3}

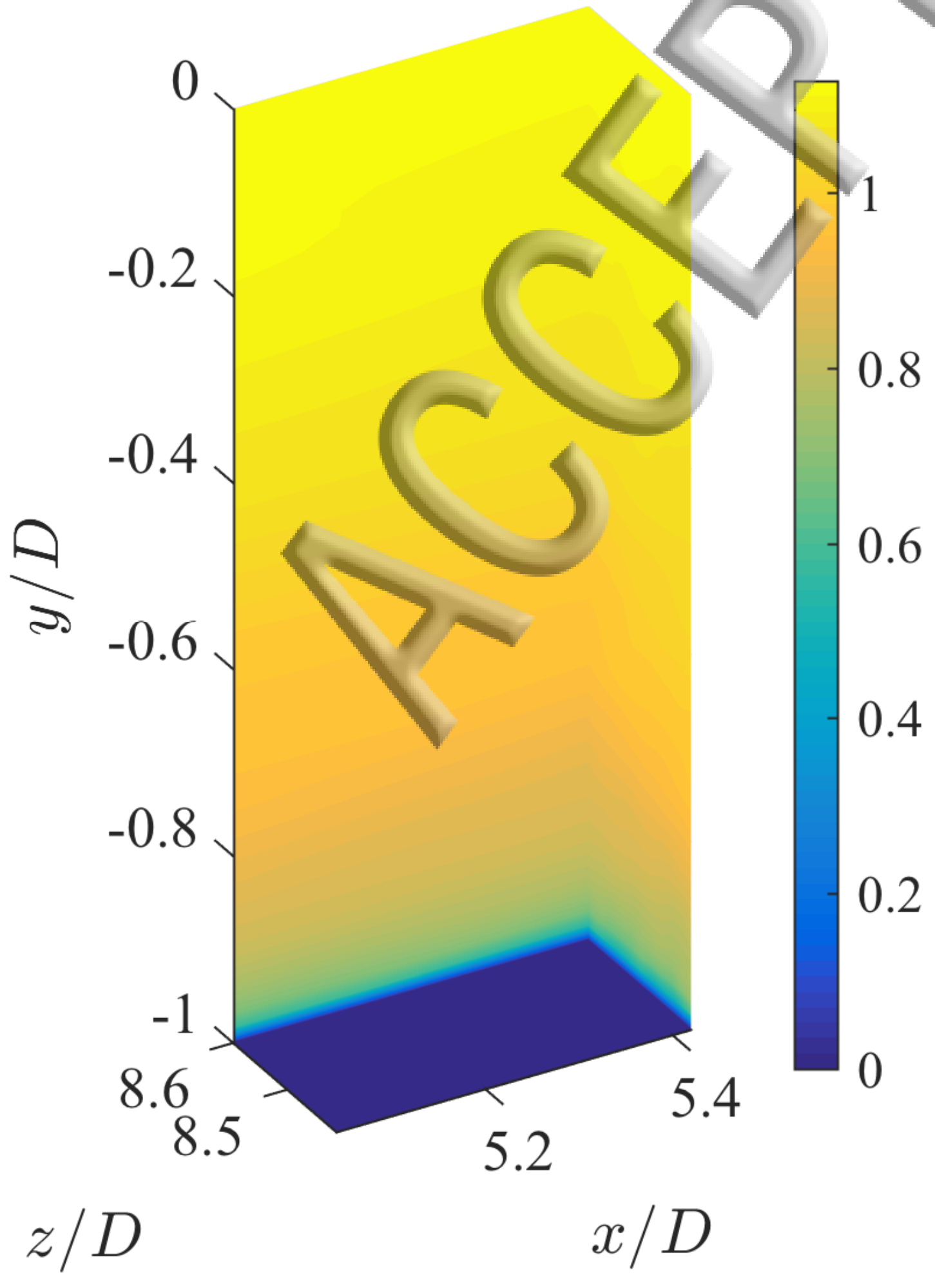

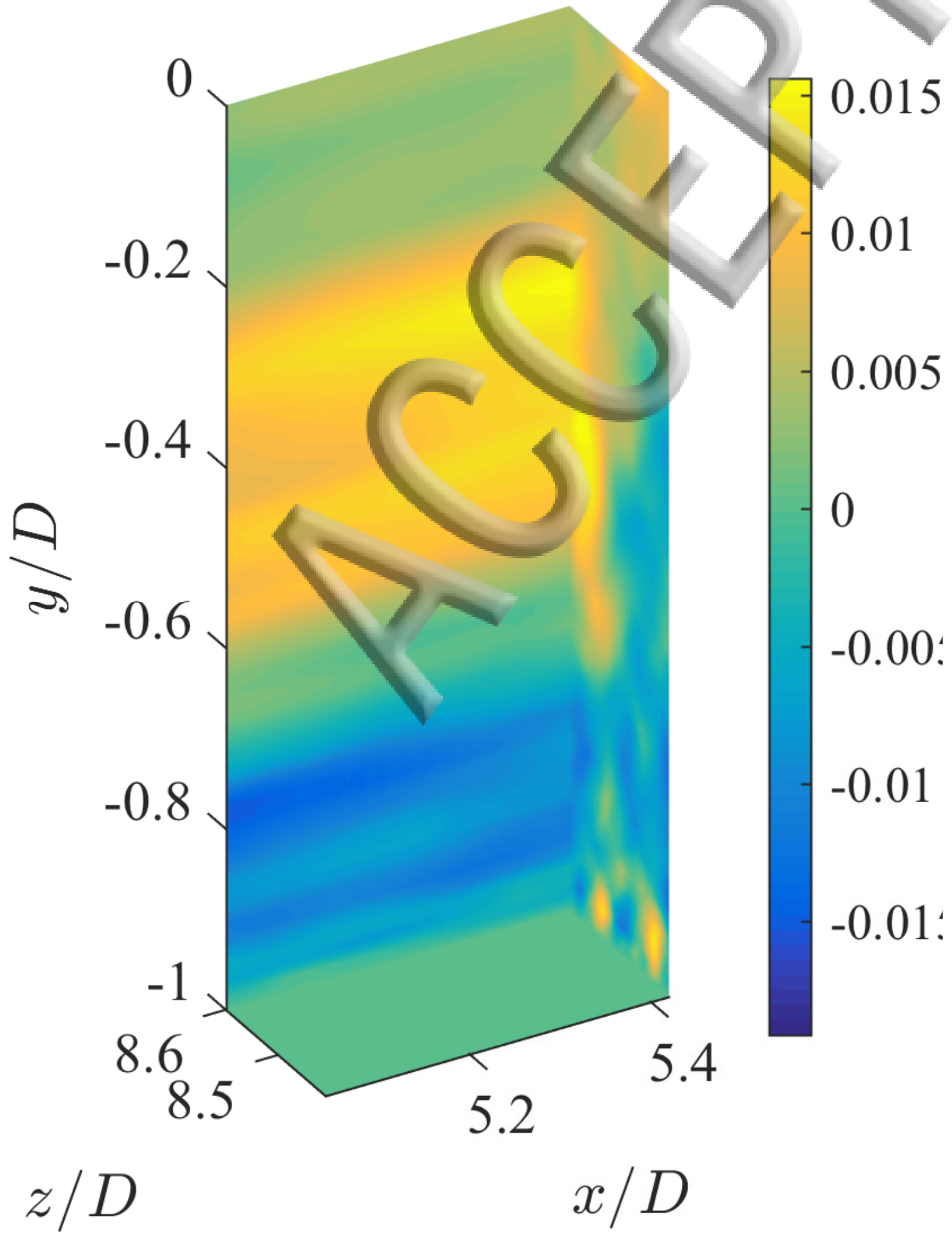
0
-0.2
-0.4
-0.6
-0.8
-1
y/D
8.6
8.5
z/D
5.2
5.4
x/D
0.015
0.01
0.005
0
-0.01

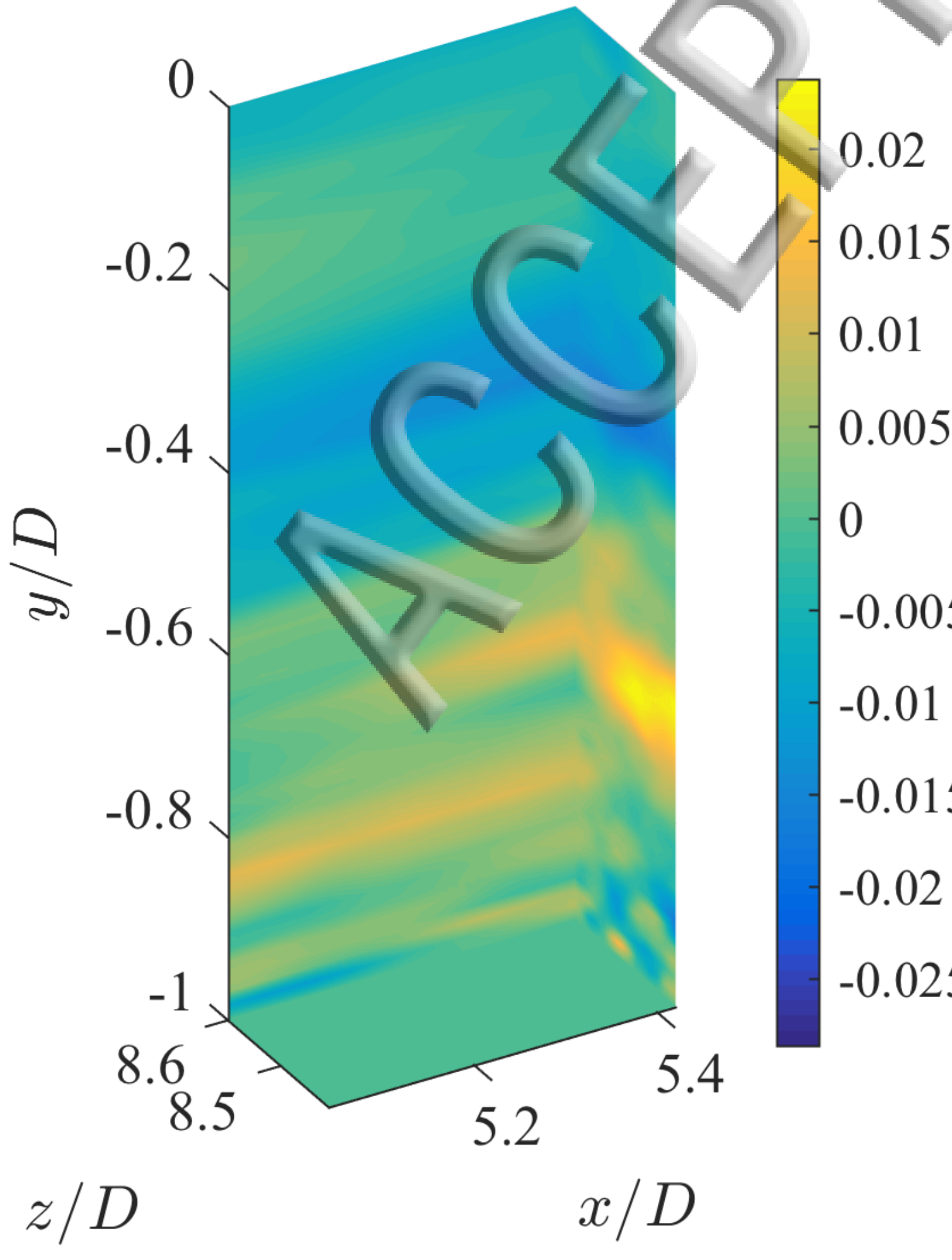
0
-0.2
-0.4
-0.6
-0.8
-1
y/D
8.6
8.5
z/D
5.2
5.4
x/D
0.02
0.015
0.01
0.005
0
-0.01
-0.02

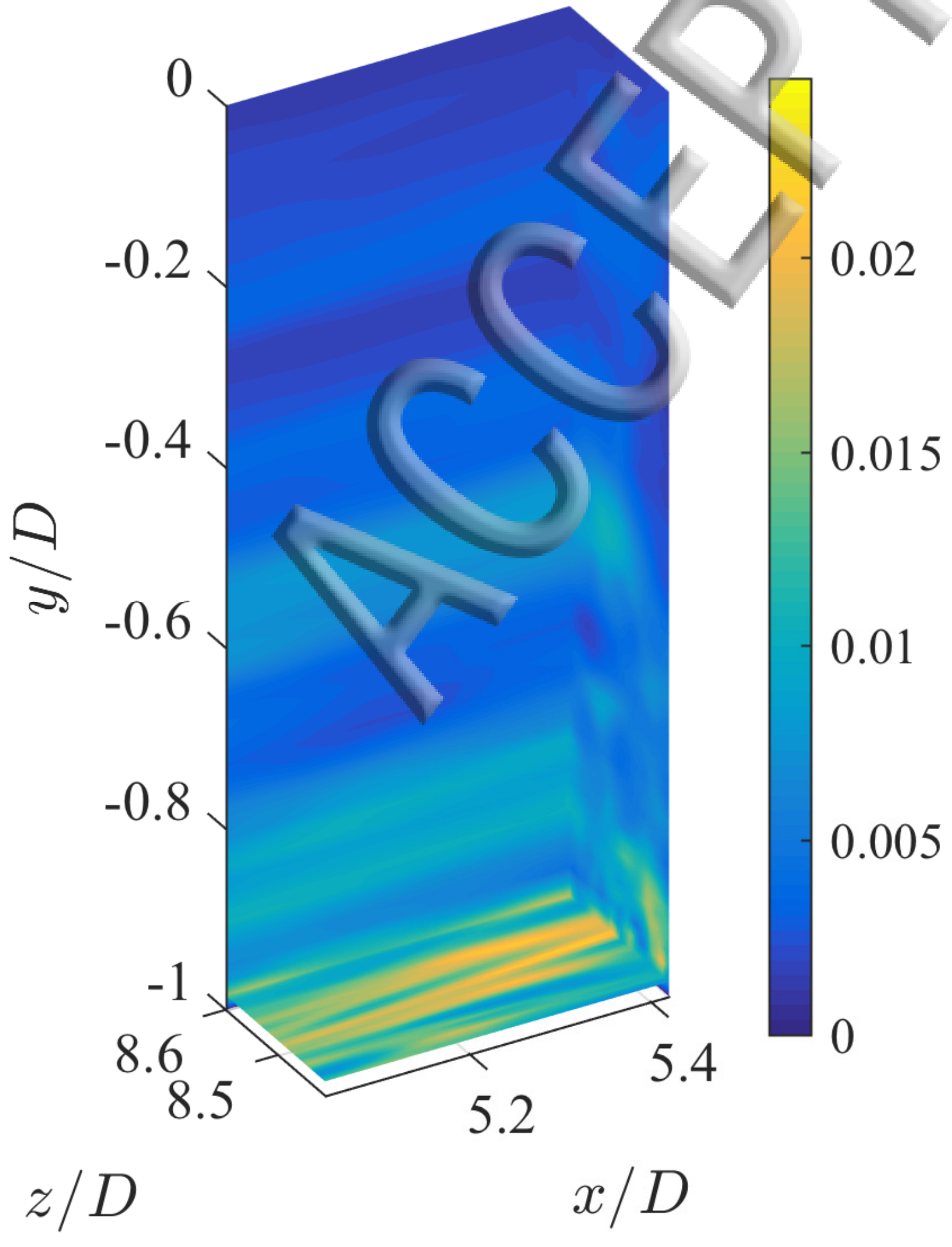
0
-0.2
-0.4
-0.6
-0.8
-1
y/D
8.6
8.5
5.2
5.4
z/D
x/D
0.02
0.015
0.01
0.005
0

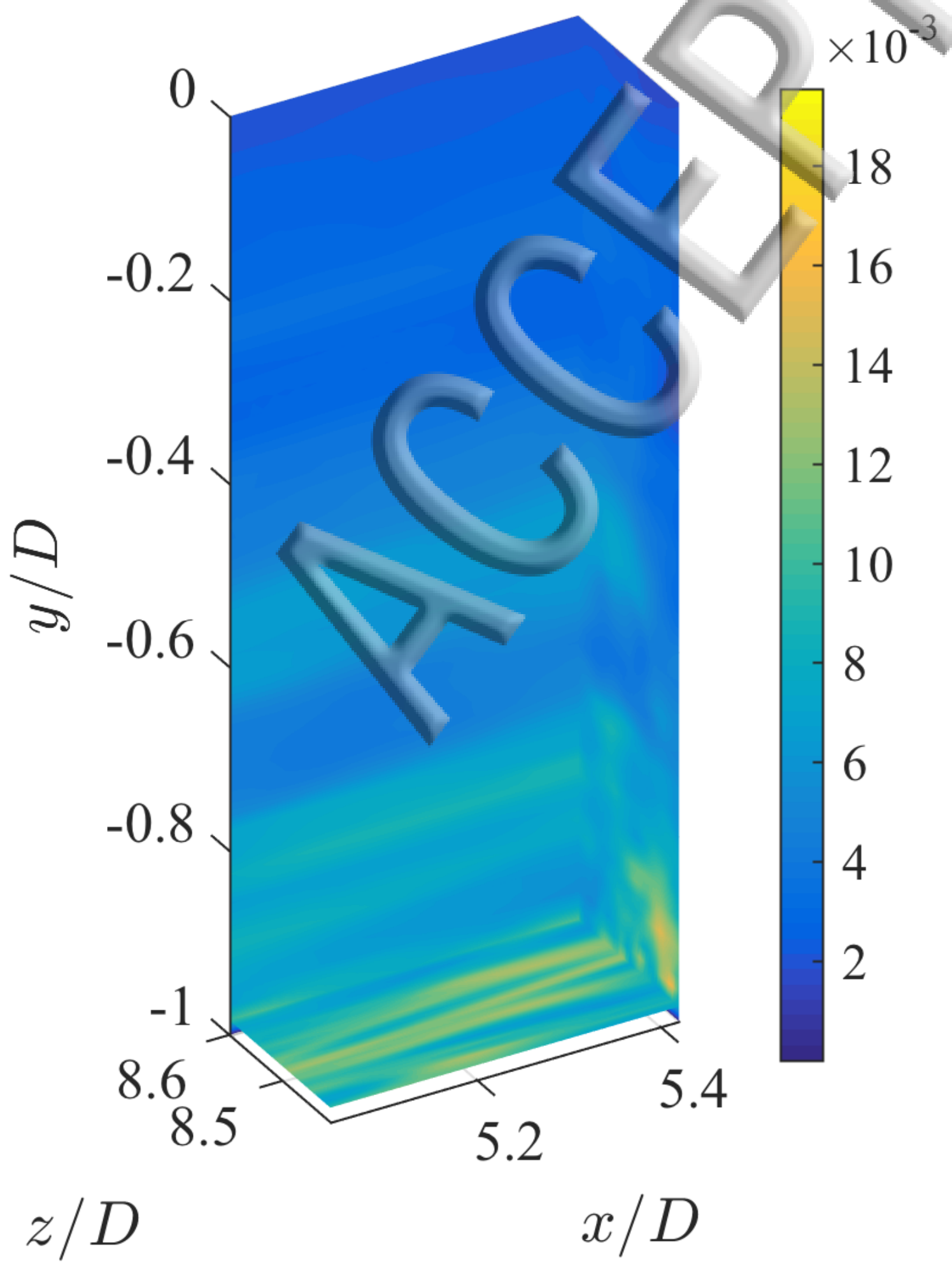
0
-0.2
-0.4
-0.6
-0.8
-1
y/D
8.6
8.5
z/D
5.2
5.4
x/D
×10^-3
18
16
14
12
10
8
6
4
2

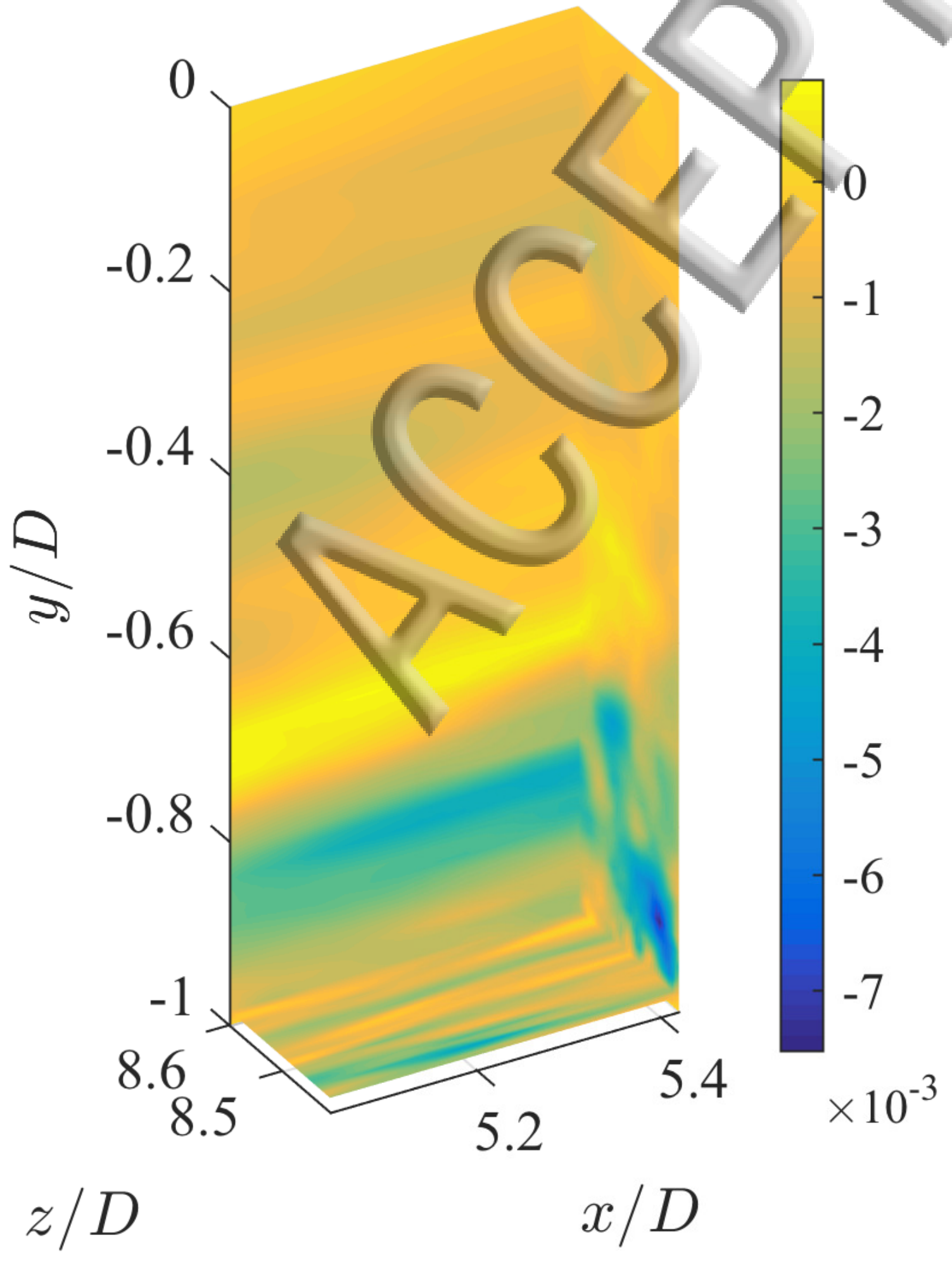

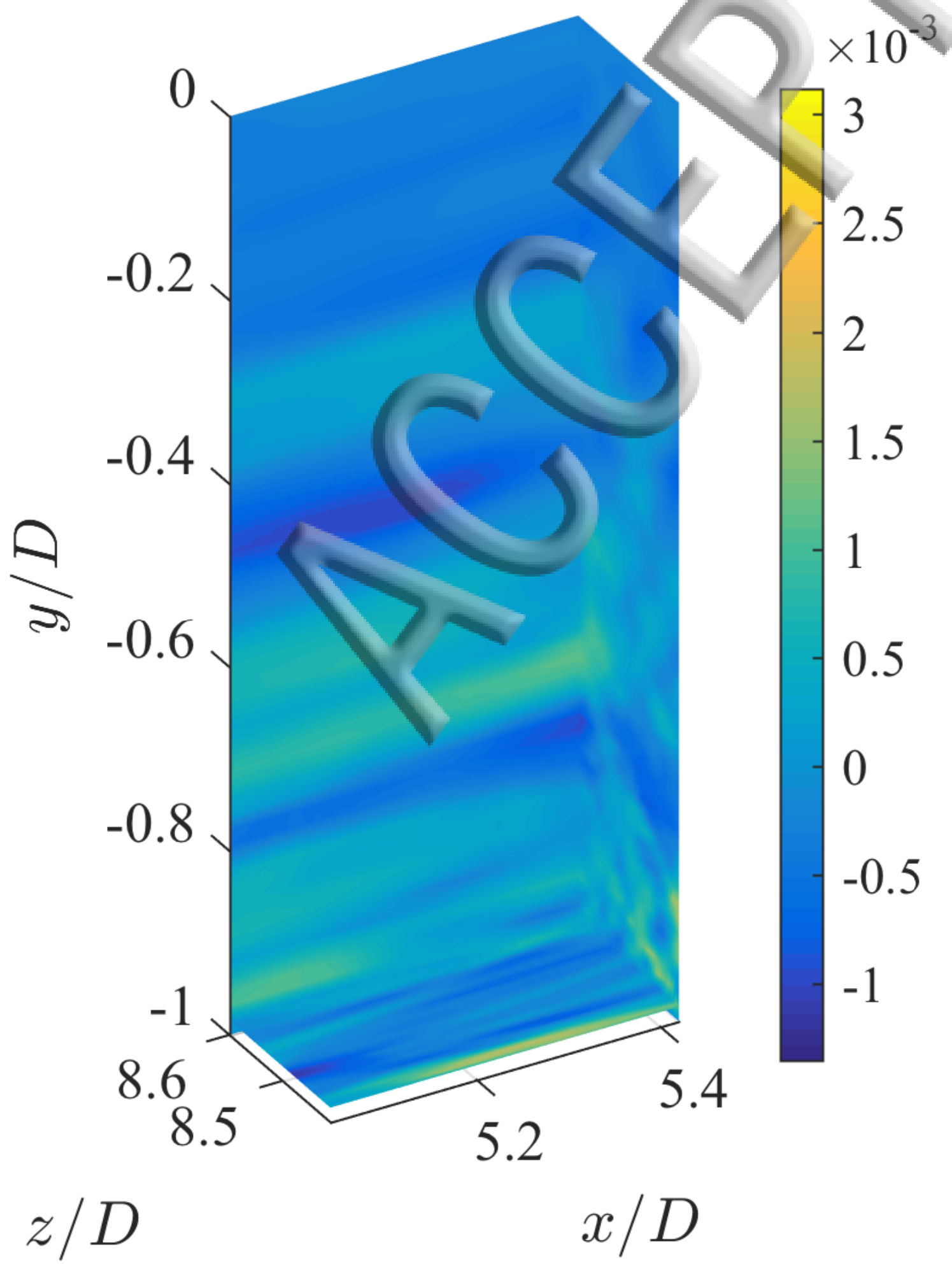

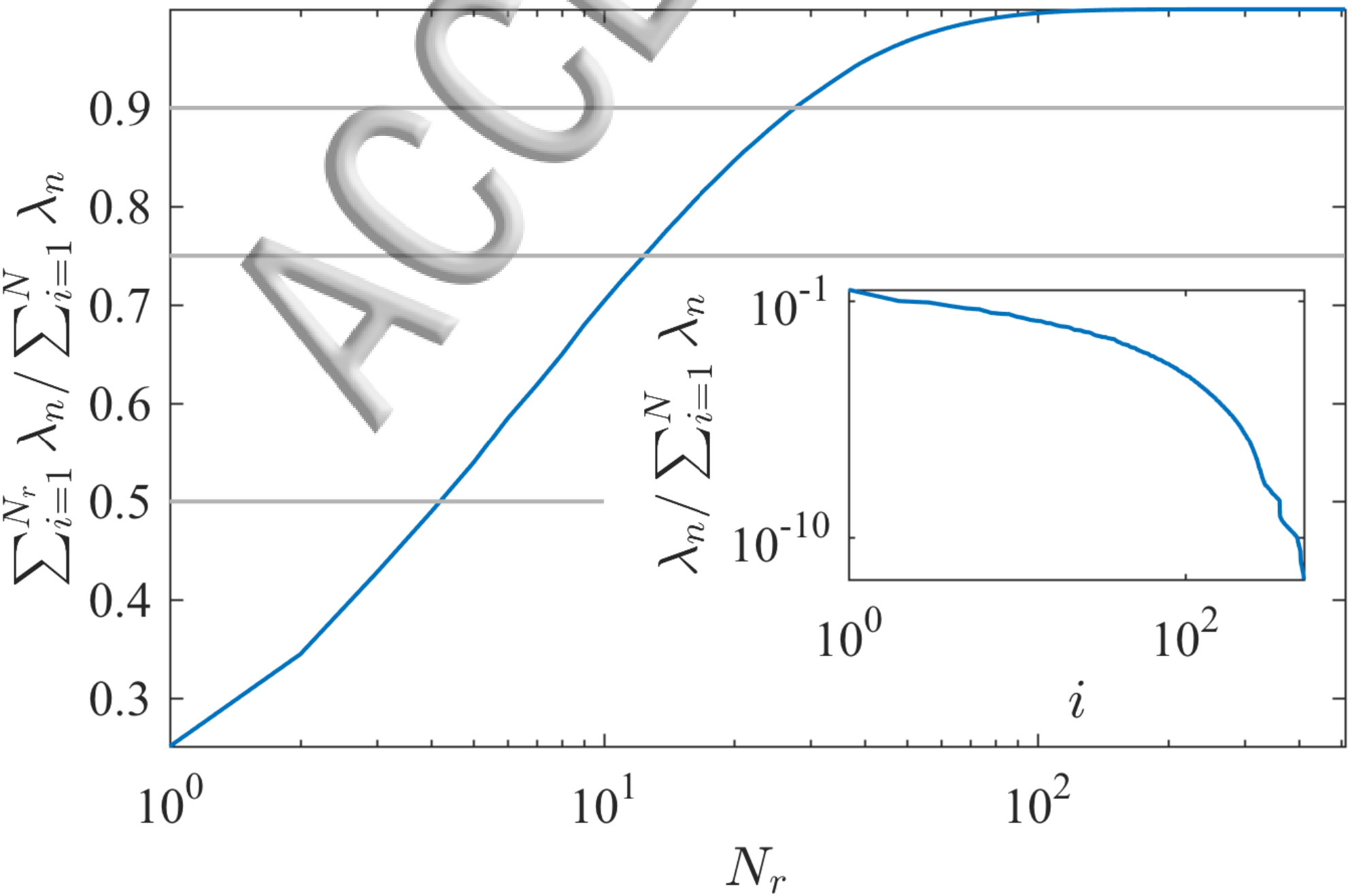
0.9
0.8
0.7
0.6
0.5
0.4
0.3
$\sum_{i=1}^{N_r} \lambda_n / \sum_{i=1}^{N} \lambda_n$
10^0
10^1
10^2
N_r
10^{-1}
10^{-10}
$\lambda_n / \sum_{i=1}^{N} \lambda_n$
10^0
10^2
i

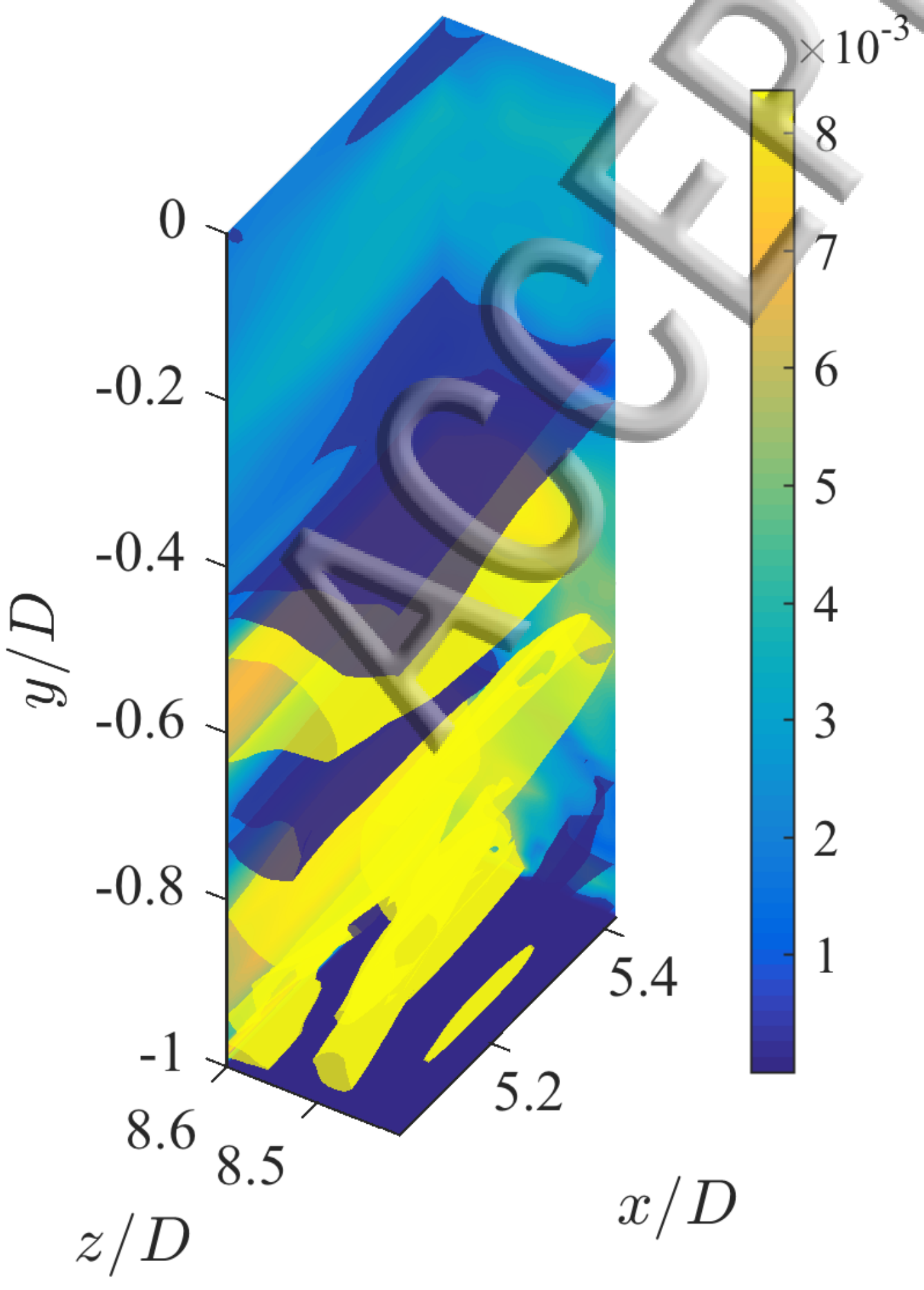

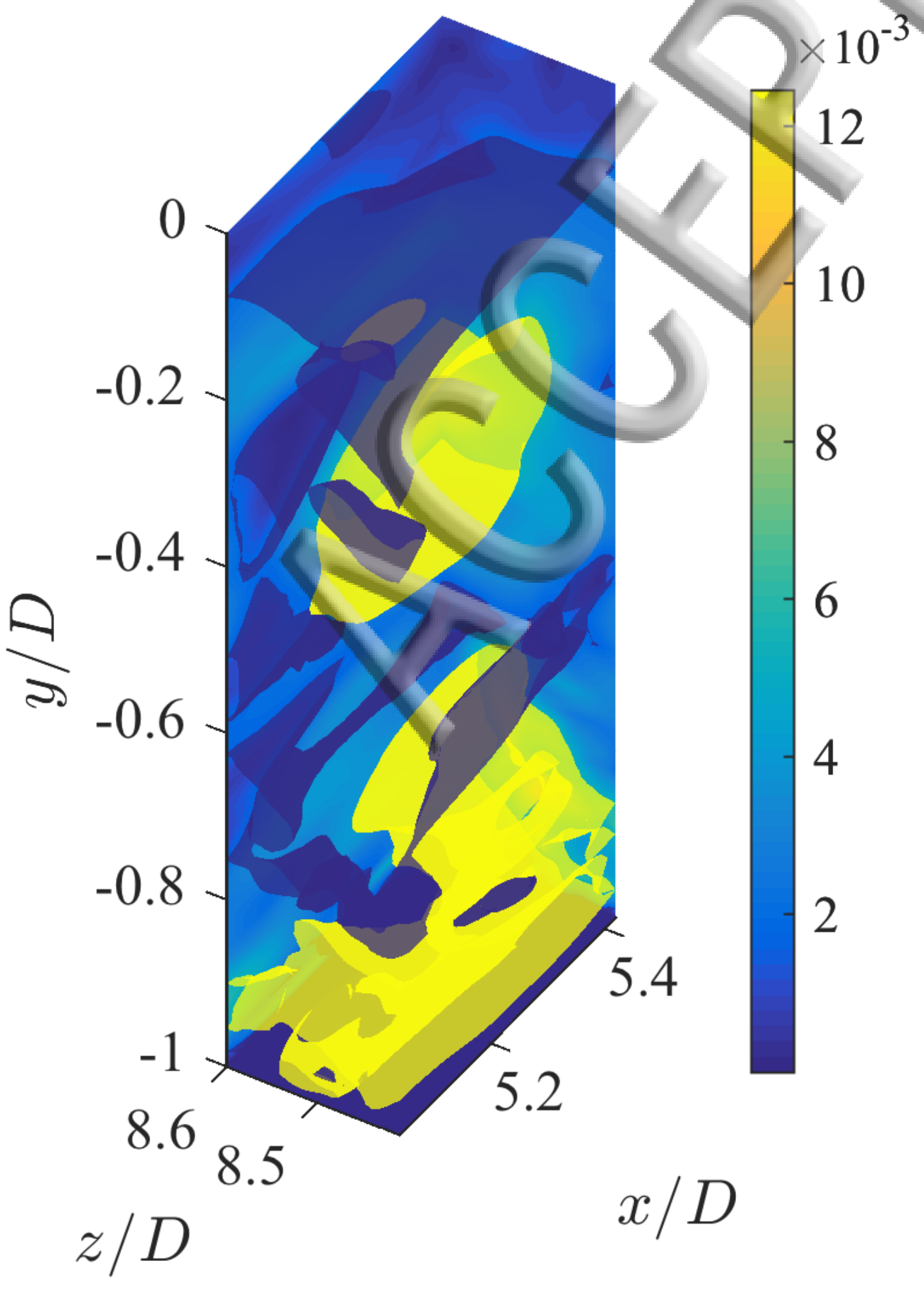
$\times 10^{-3}$
12
10
8
6
4
2
0
-0.2
-0.4
-0.6
-0.8
-1
y/D
8.6
8.5
z/D
5.2
5.4
x/D

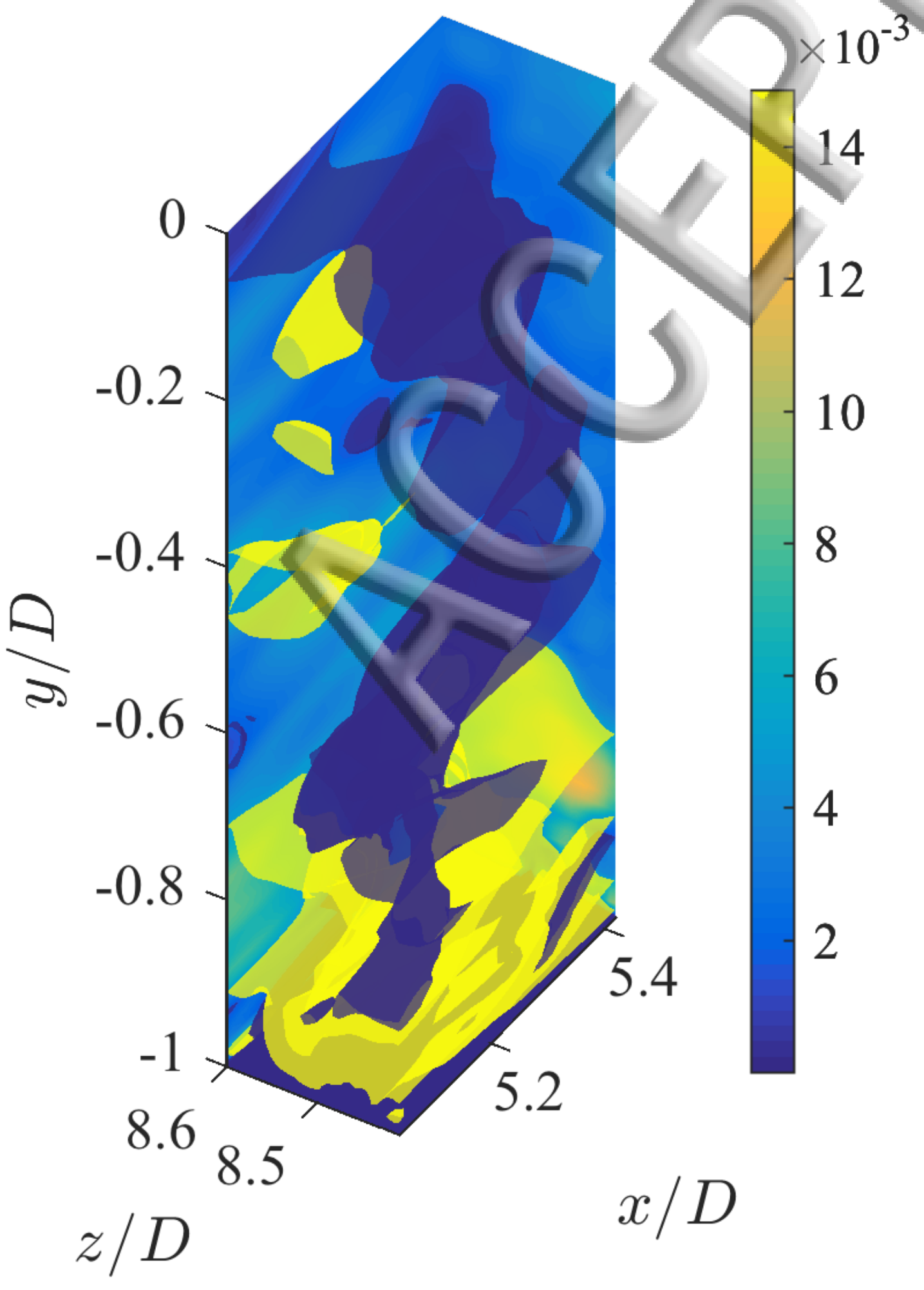

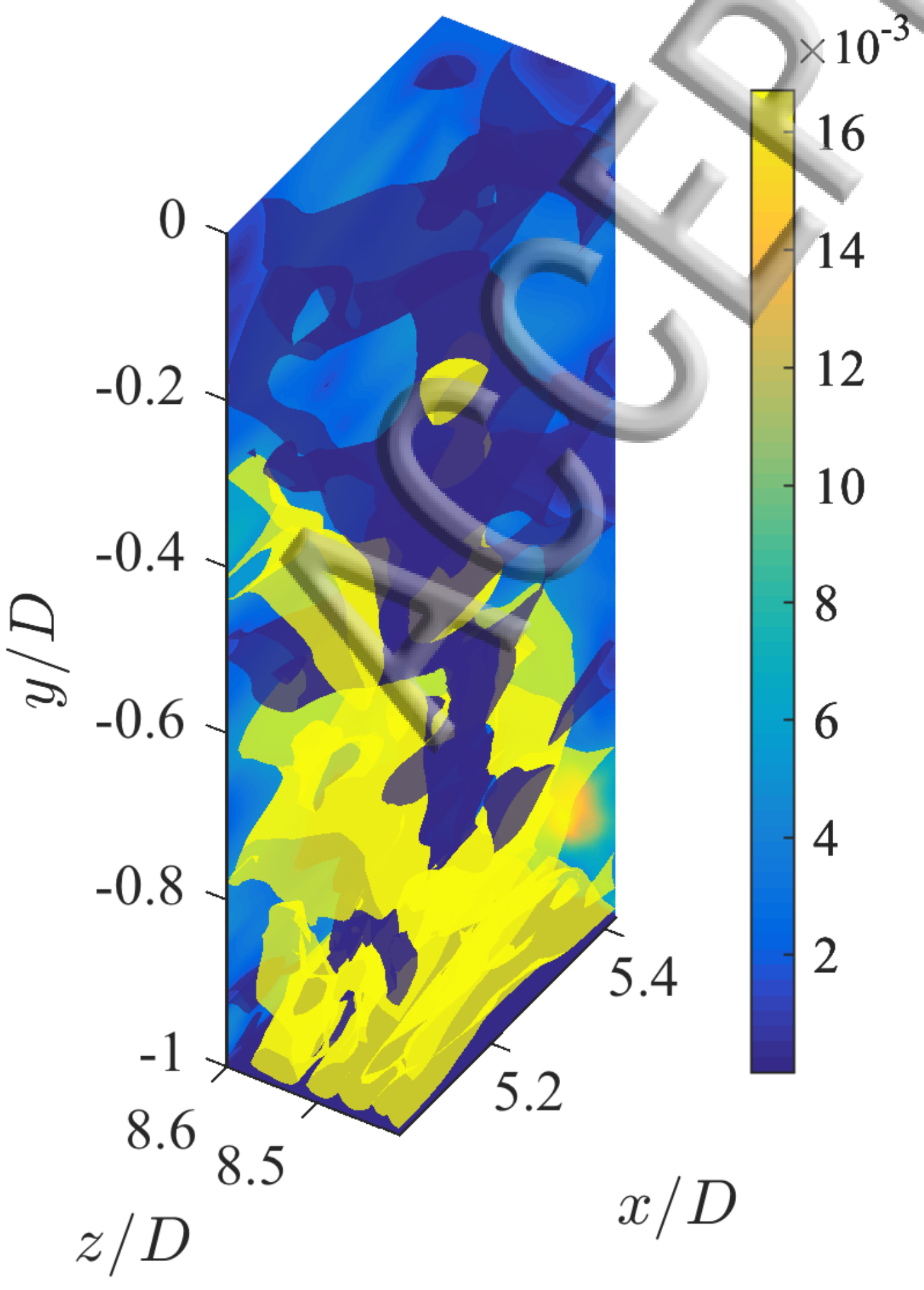
$\times 10^{-3}$
16
14
12
10
8
6
4
2
0
-0.2
-0.4
-0.6
-0.8
-1
y/D
8.6
8.5
z/D
5.2
5.4
x/D

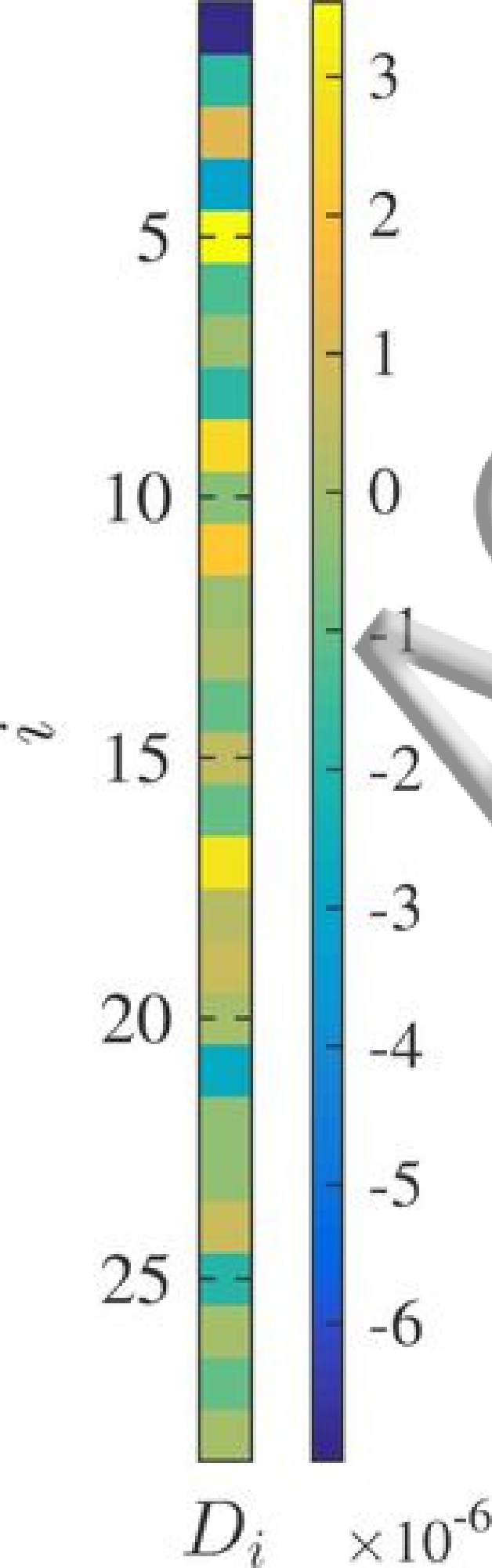
5
10
15
20
25
z
3
2
1
0
-1
-2
-3
-4
-5
-6
D_i
$\times 10^{-6}$

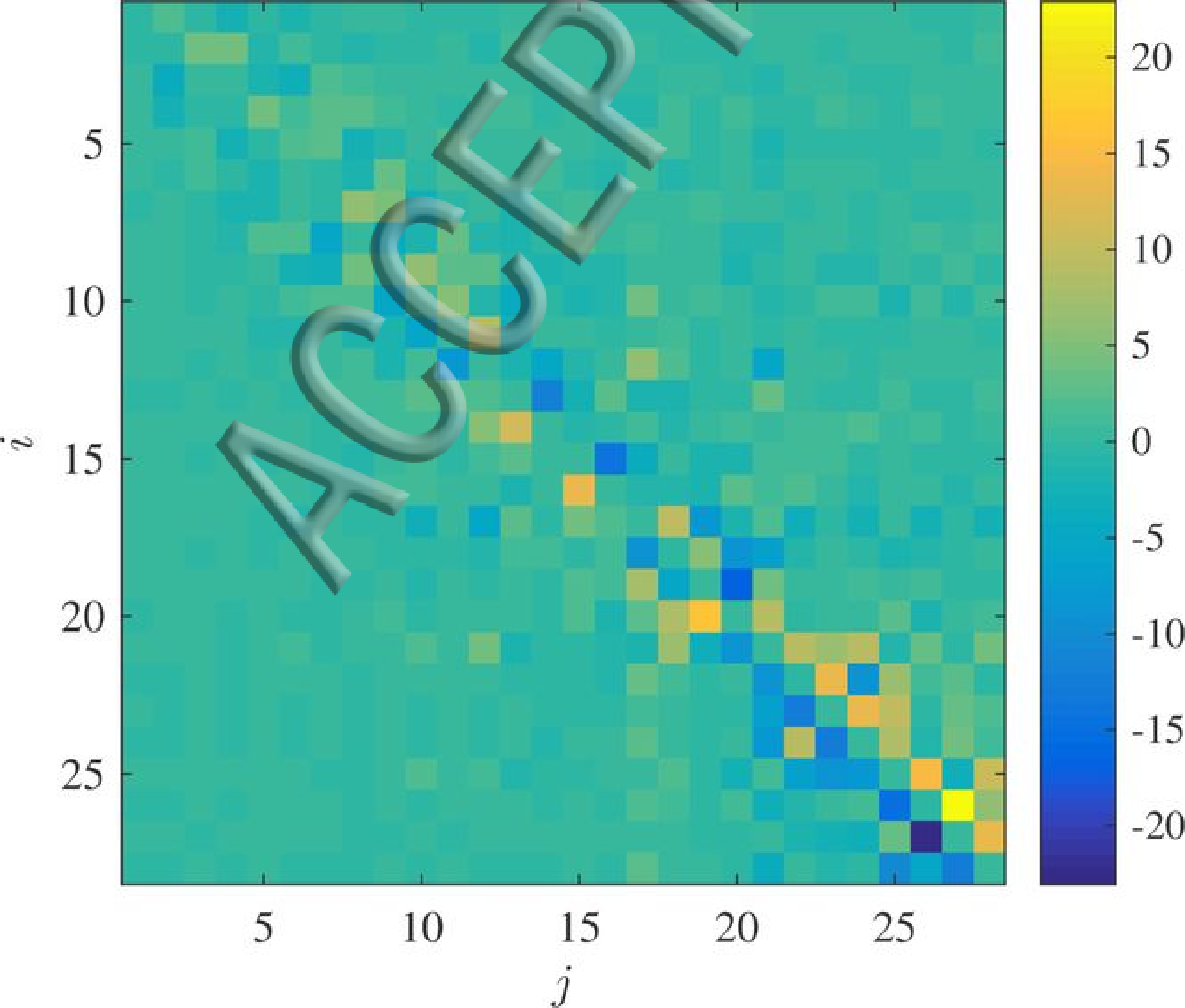

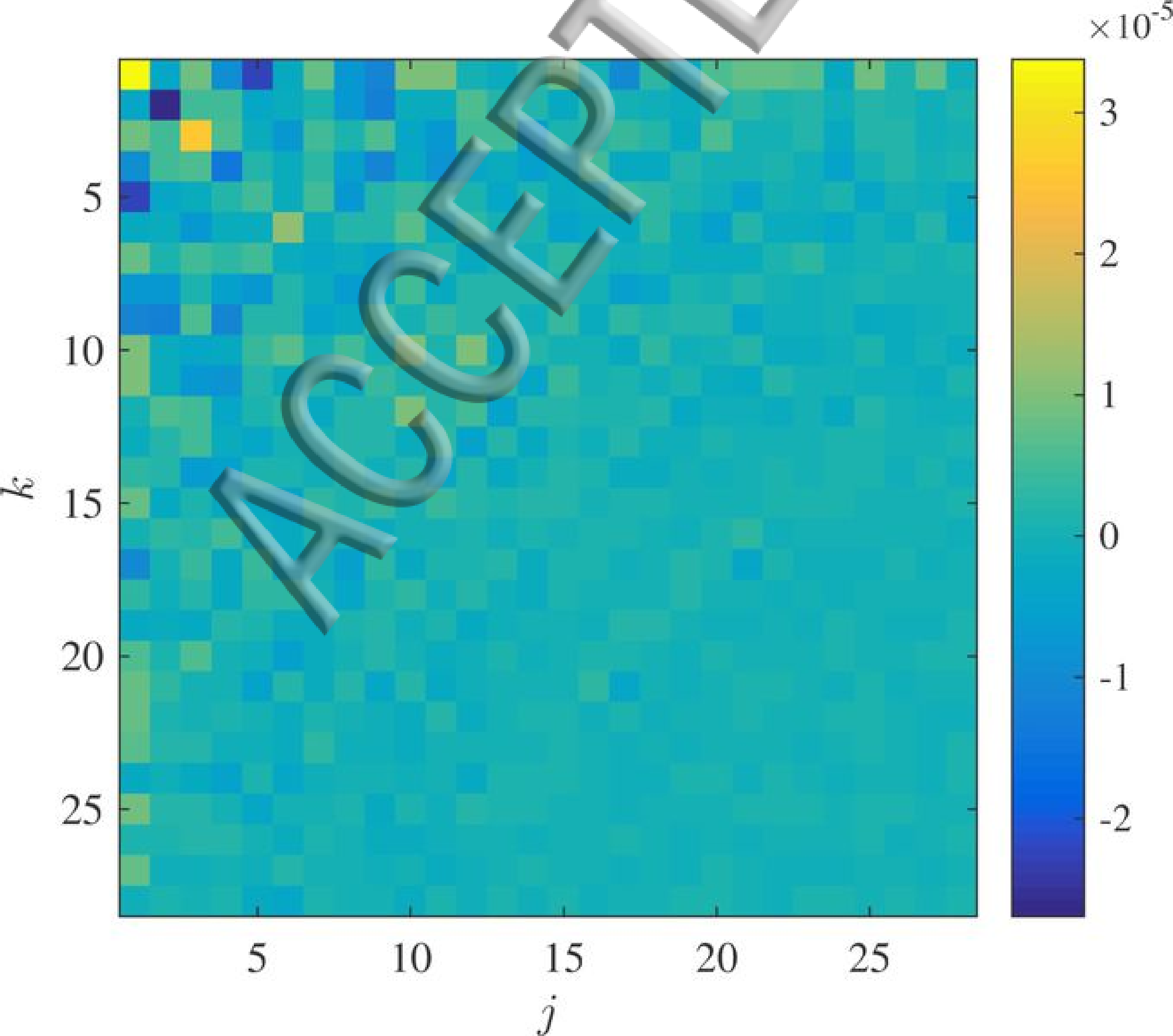

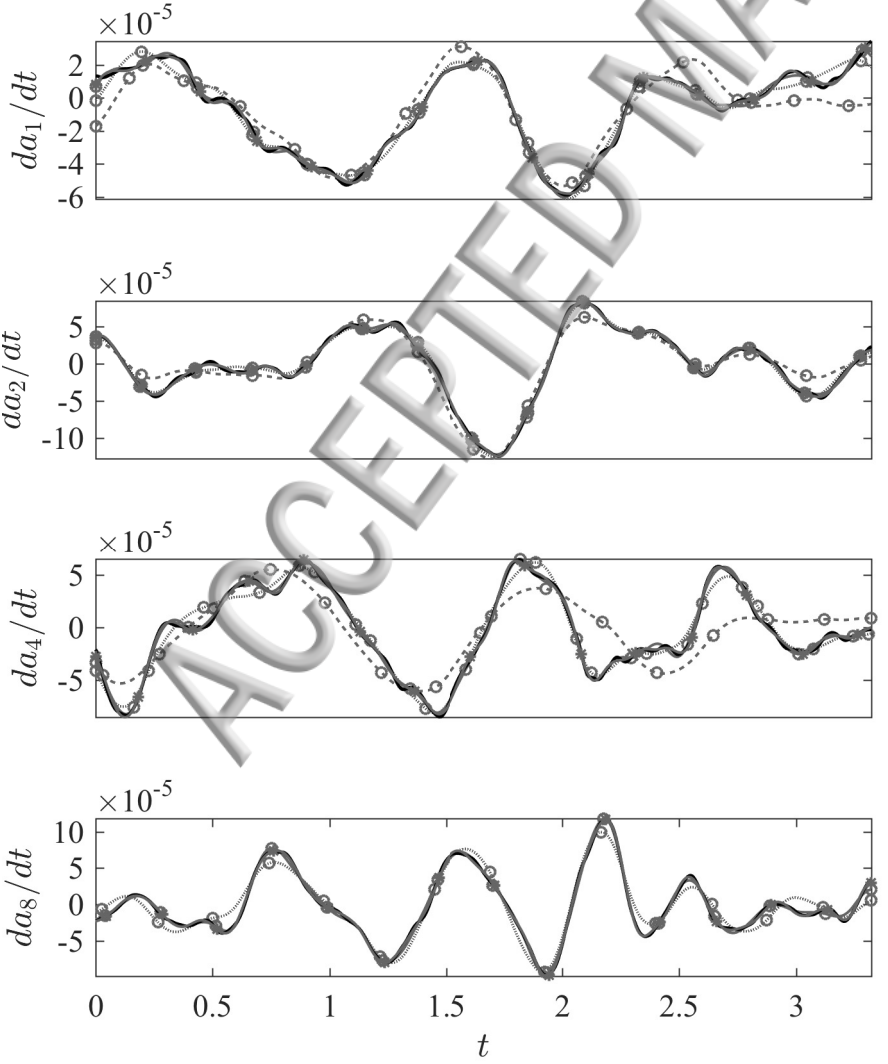
×10^-5
da1/dt
2
0
-2
-4
-6
×10^-5
da2/dt
5
0
-5
-10
×10^-5
da4/dt
5
0
-5
×10^-5
da8/dt
10
5
0
-5
0
0.5
1
1.5
2
2.5
3
t

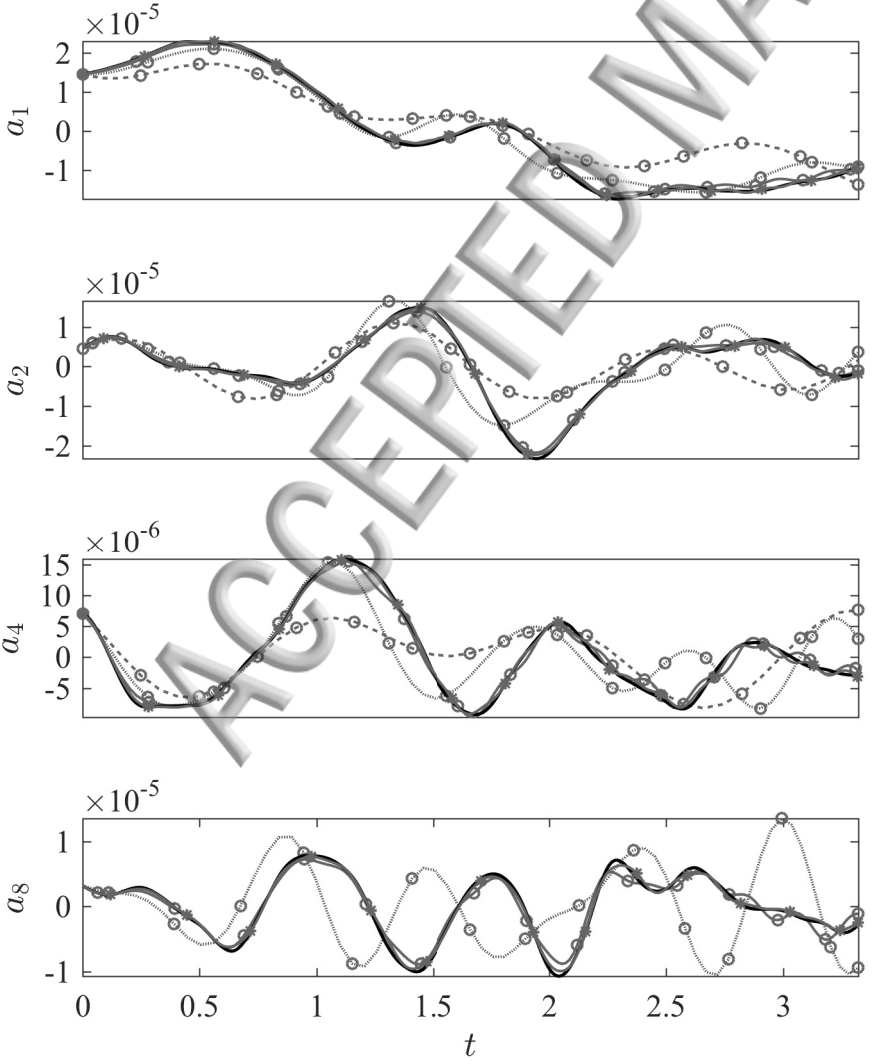
$\times 10^{-5}$
a_1
2
1
0
-1
$\times 10^{-5}$
a_2
1
0
-1
-2
$\times 10^{-6}$
a_4
15
10
5
0
-5
$\times 10^{-5}$
a_8
1
0
-1
0
0.5
1
1.5
2
2.5
3
t

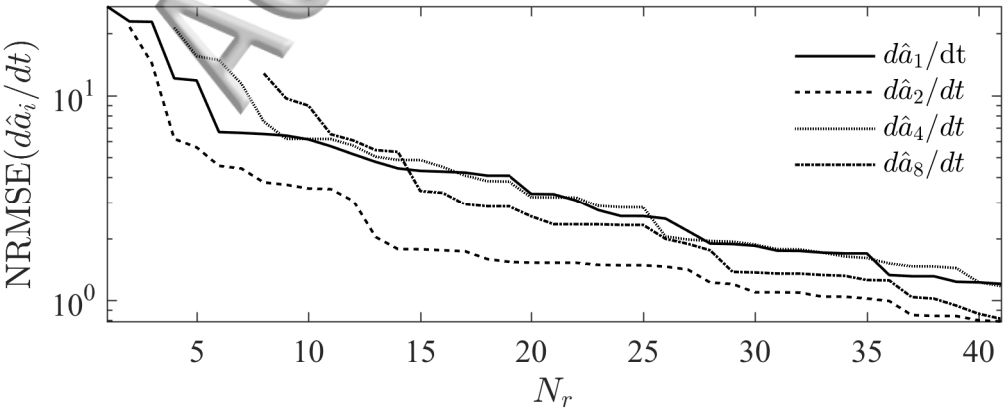
NRMSE($d\hat{a}_i/dt$)
10^1
10^0
5
10
15
20
25
30
35
40
N_r
$d\hat{a}_1/\mathrm{dt}$
$d\hat{a}_2/dt$
$d\hat{a}_4/dt$
$d\hat{a}_8/dt$

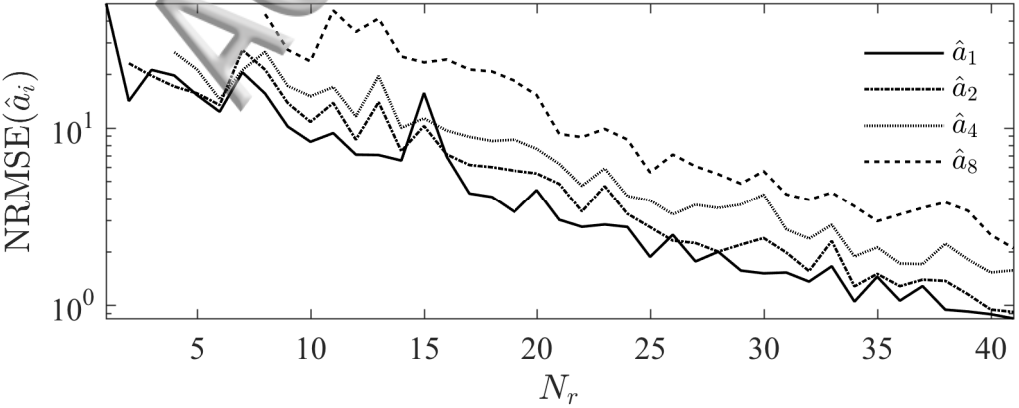
NRMSE($\hat{a}_i$)
10^1
10^0
5
10
15
20
25
30
35
40
N_r
$\hat{a}_1$
$\hat{a}_2$
$\hat{a}_4$
$\hat{a}_8$

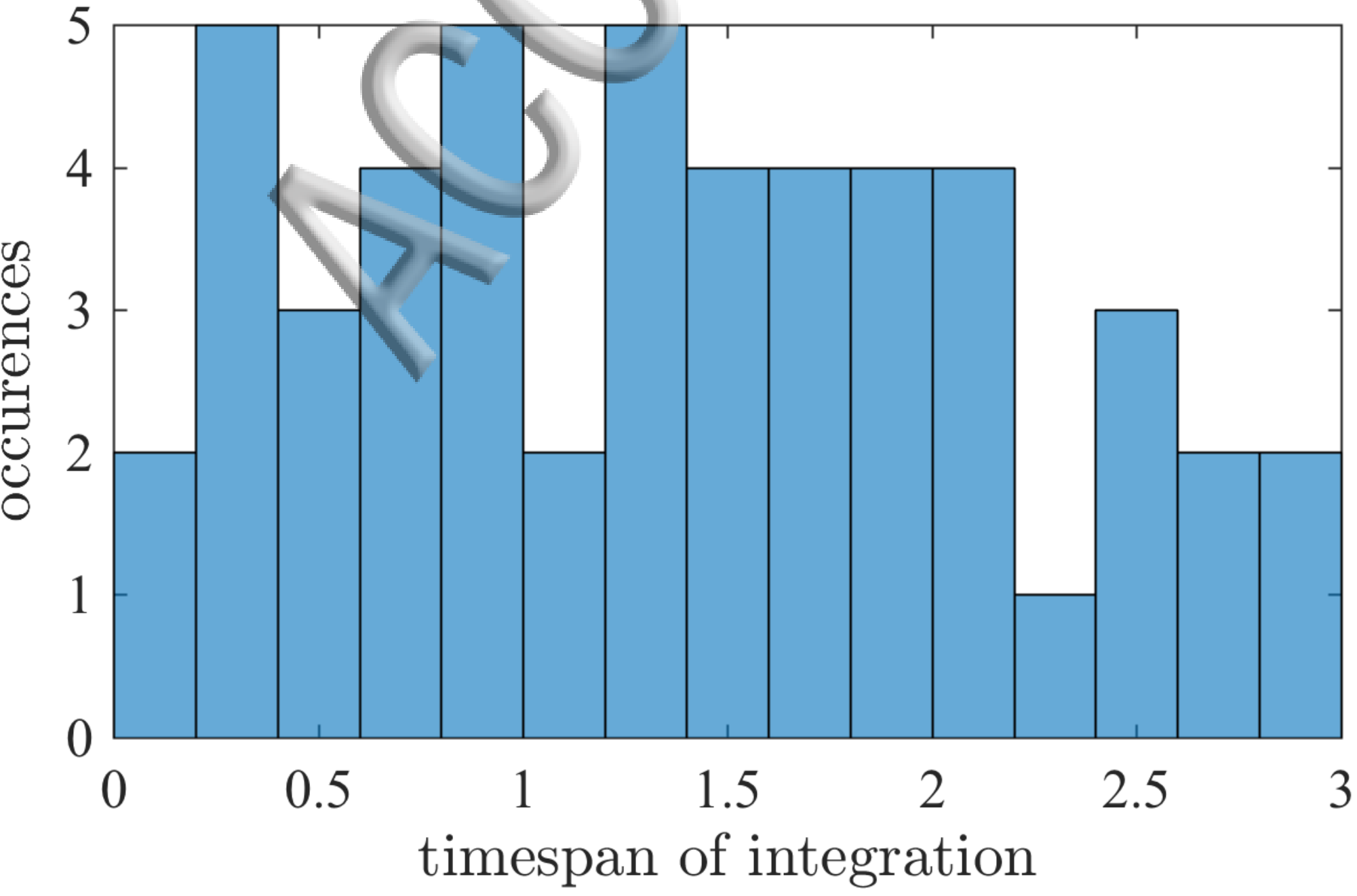
occurences
timespan of integration
0
1
2
3
4
5
0
0.5
1
1.5
2
2.5
3

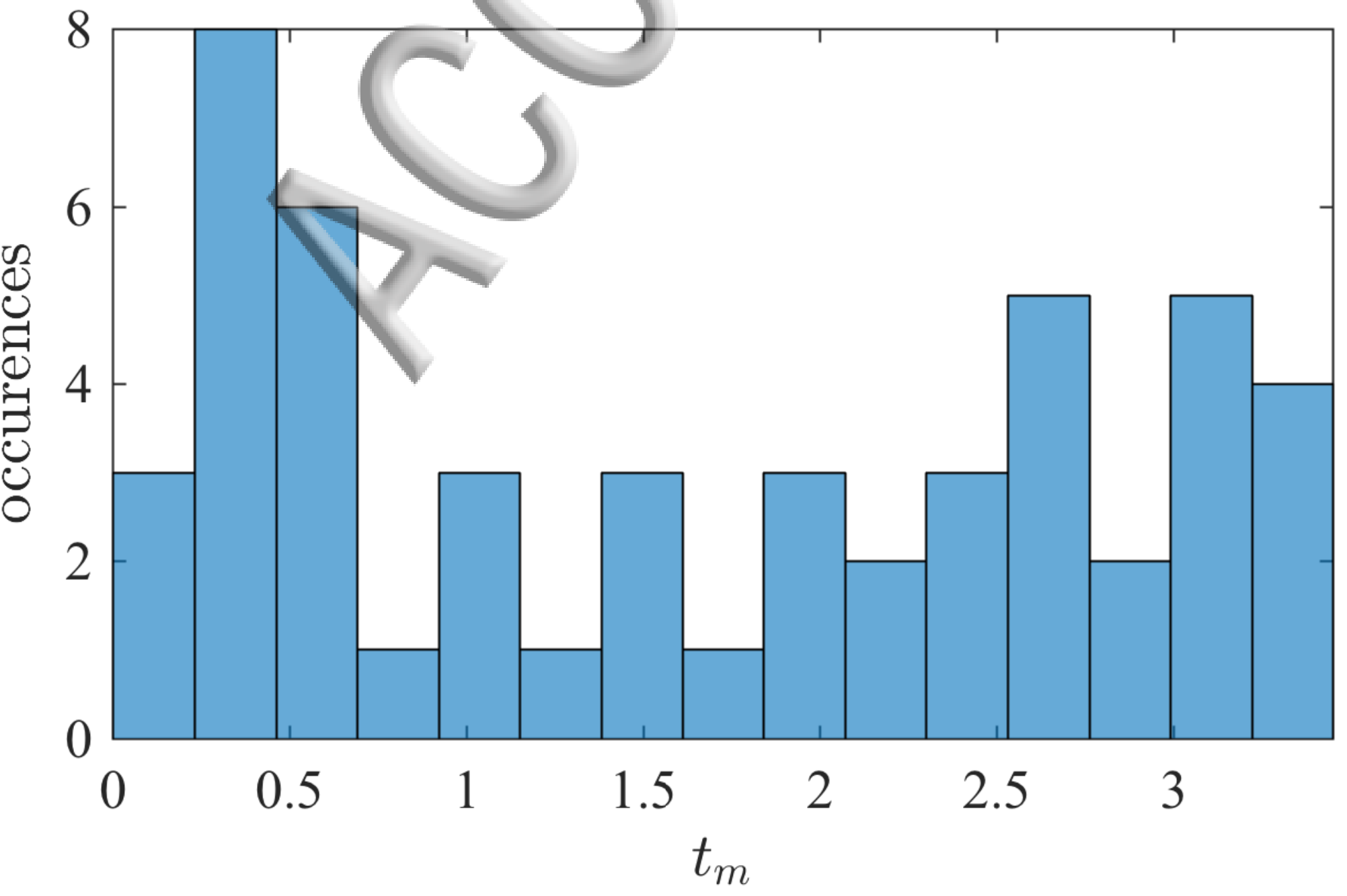
occurences
0
2
4
6
8
0
0.5
1
1.5
2
2.5
3
t_m

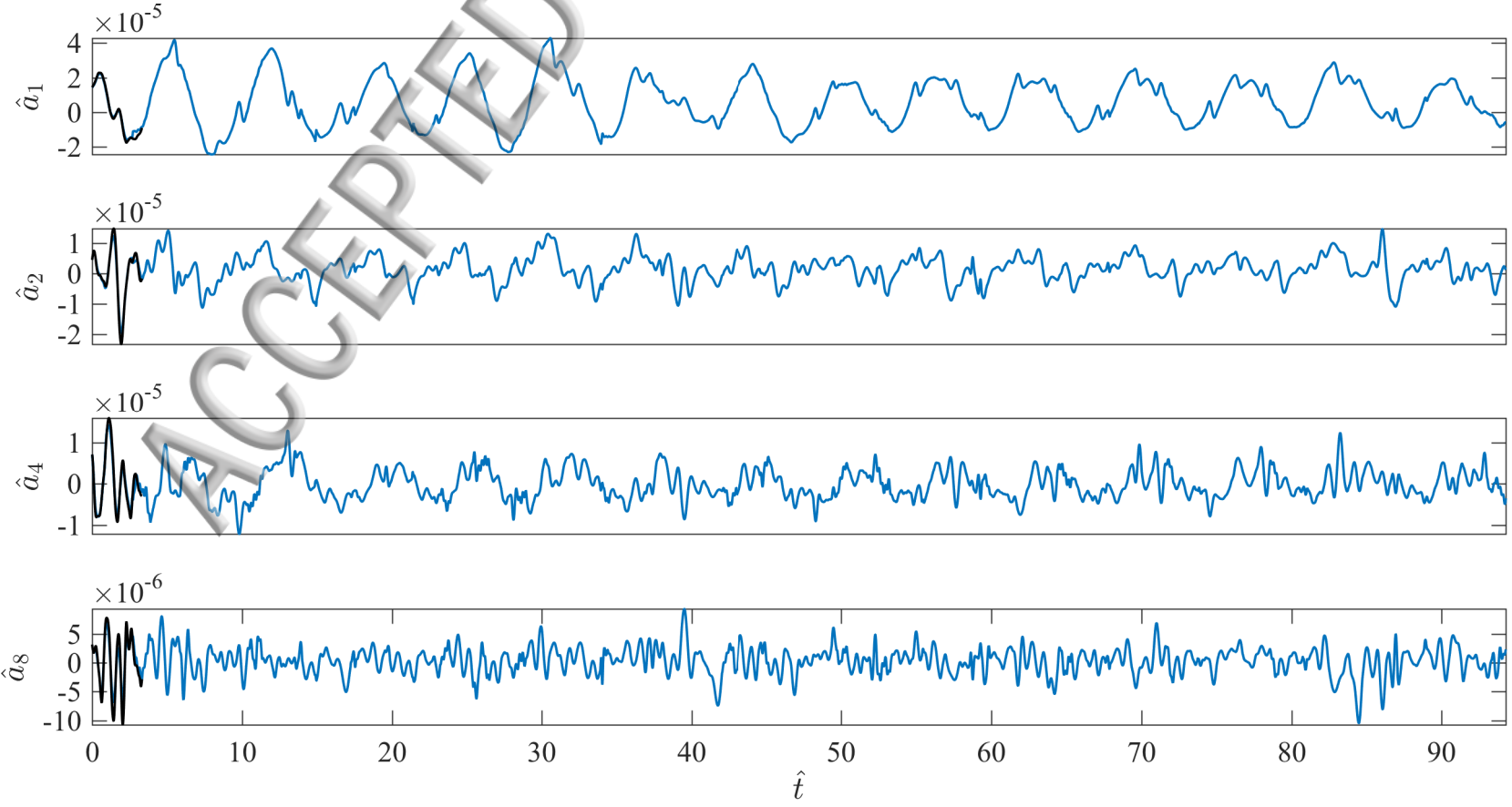
$\times 10^{-5}$
$\hat{a}_1$
4
2
0
-2
$\times 10^{-5}$
$\hat{a}_2$
1
0
-1
-2
$\times 10^{-5}$
$\hat{a}_4$
1
0
-1
$\times 10^{-6}$
$\hat{a}_8$
5
0
-5
-10
0
10
20
30
40
50
60
70
80
90
$\hat{t}$

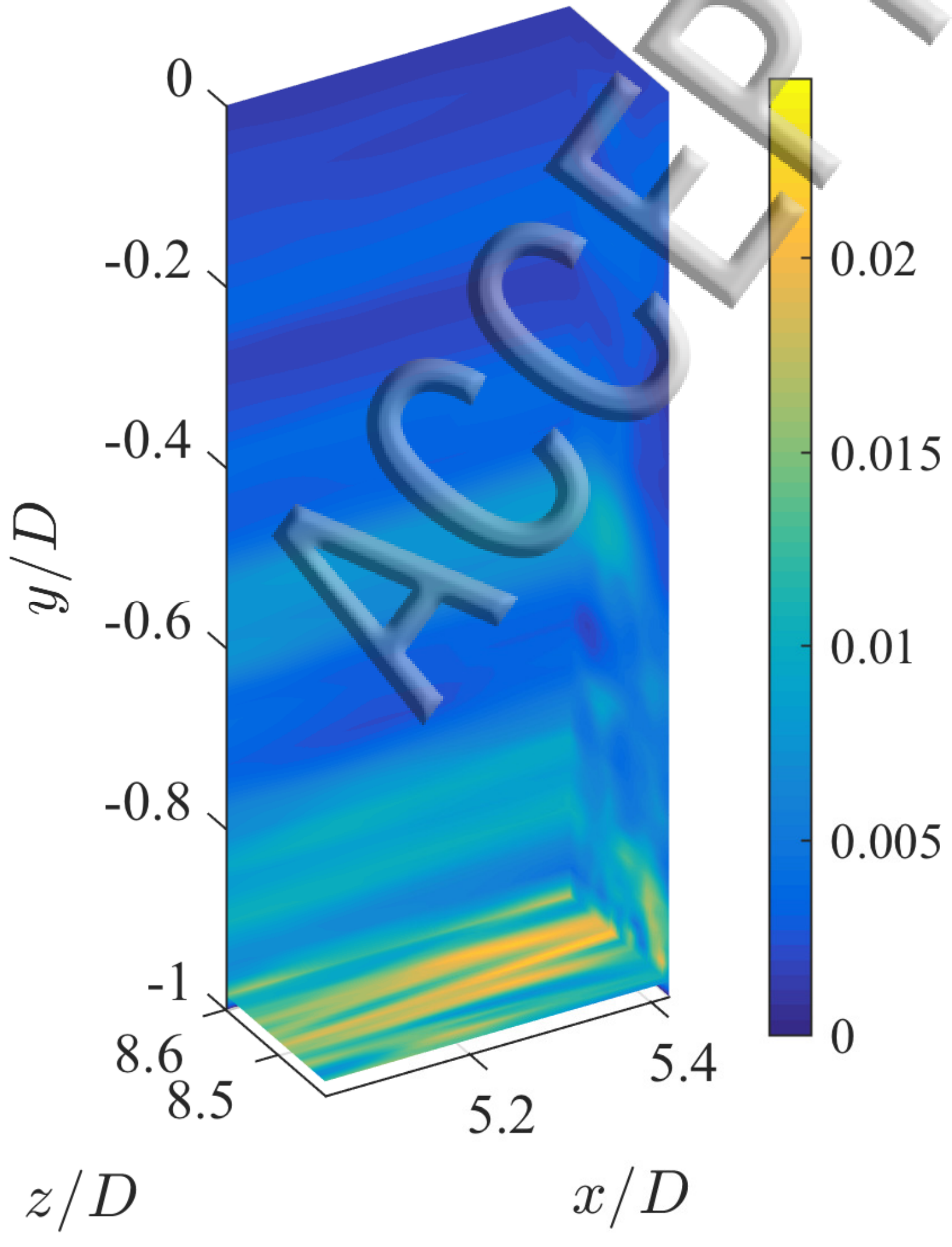
0
-0.2
-0.4
-0.6
-0.8
-1
y/D
8.6
8.5
5.2
5.4
z/D
x/D
0.02
0.015
0.01
0.005
0

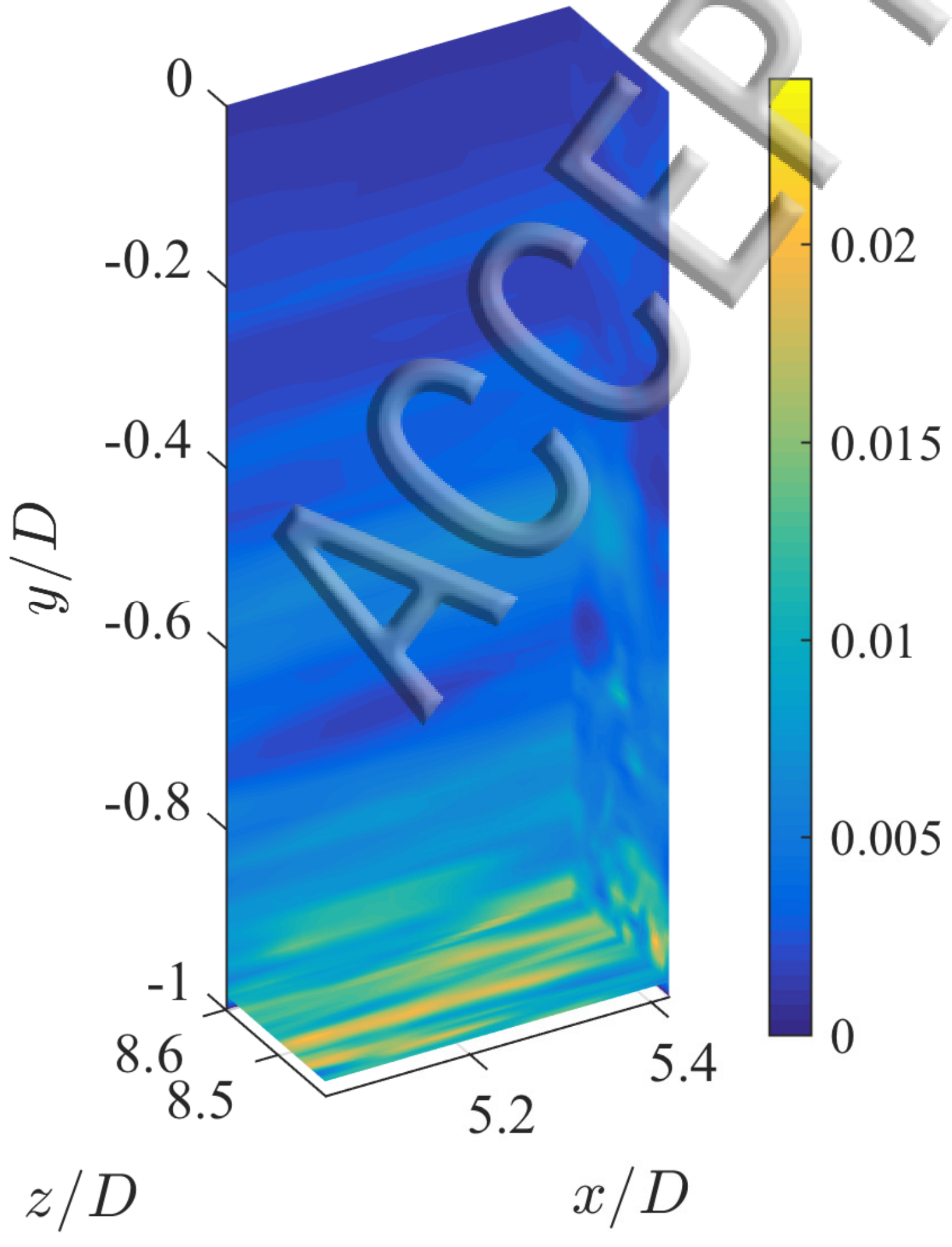
0
-0.2
-0.4
-0.6
-0.8
-1
y/D
8.6
8.5
5.2
5.4
z/D
x/D
0.02
0.015
0.01
0.005
0

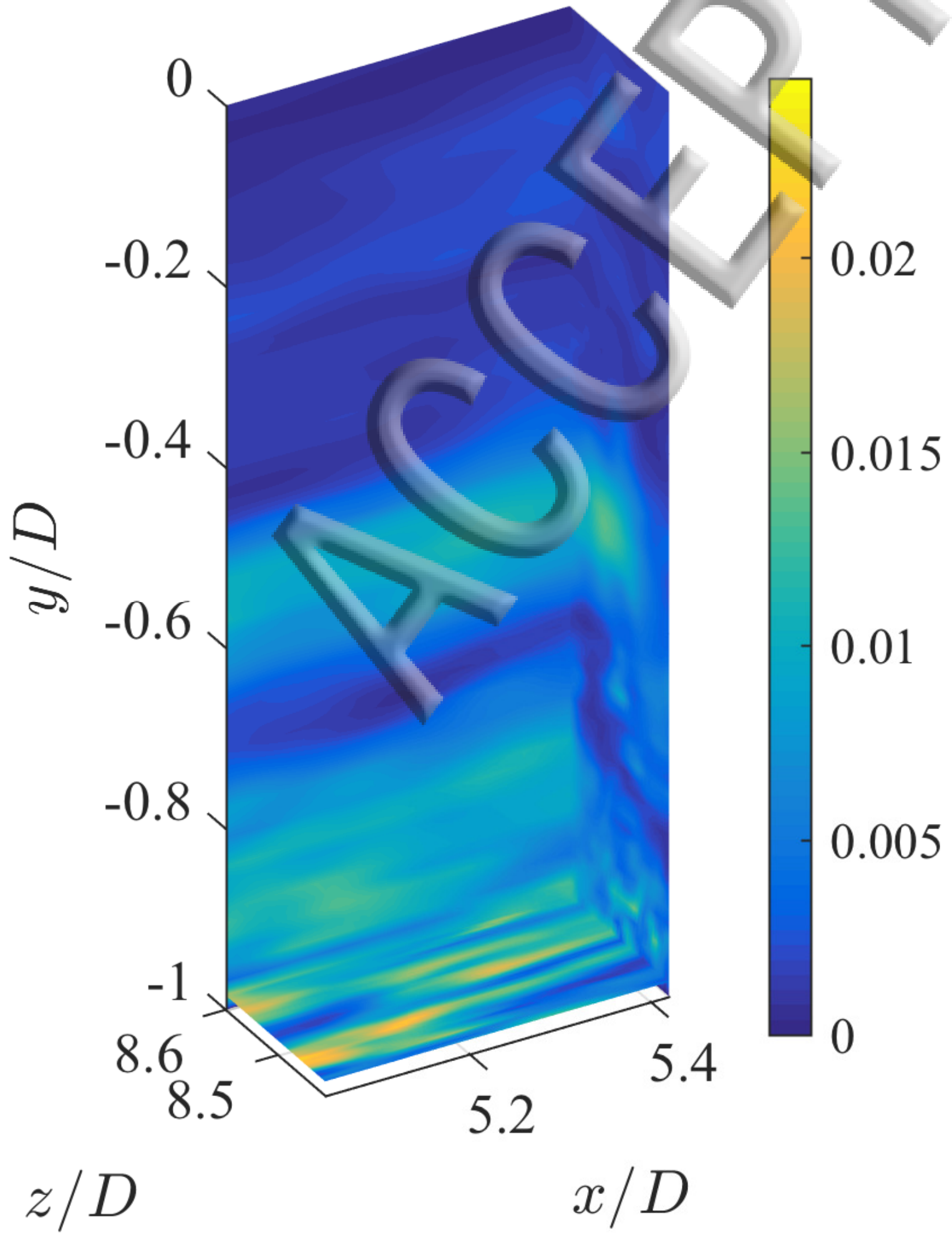
0
-0.2
-0.4
-0.6
-0.8
-1
y/D
8.6
8.5
5.2
5.4
z/D
x/D
0.02
0.015
0.01
0.005
0

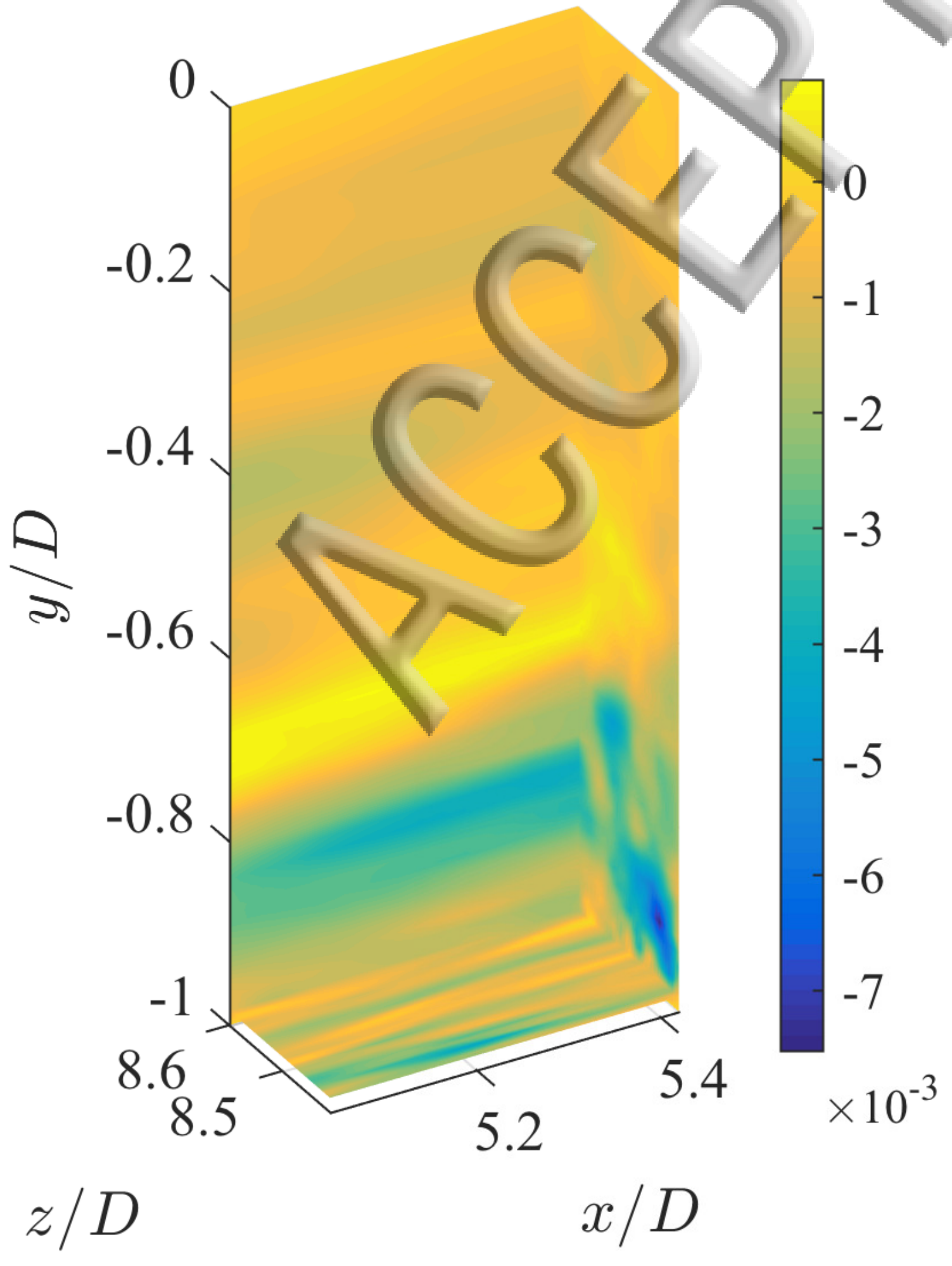

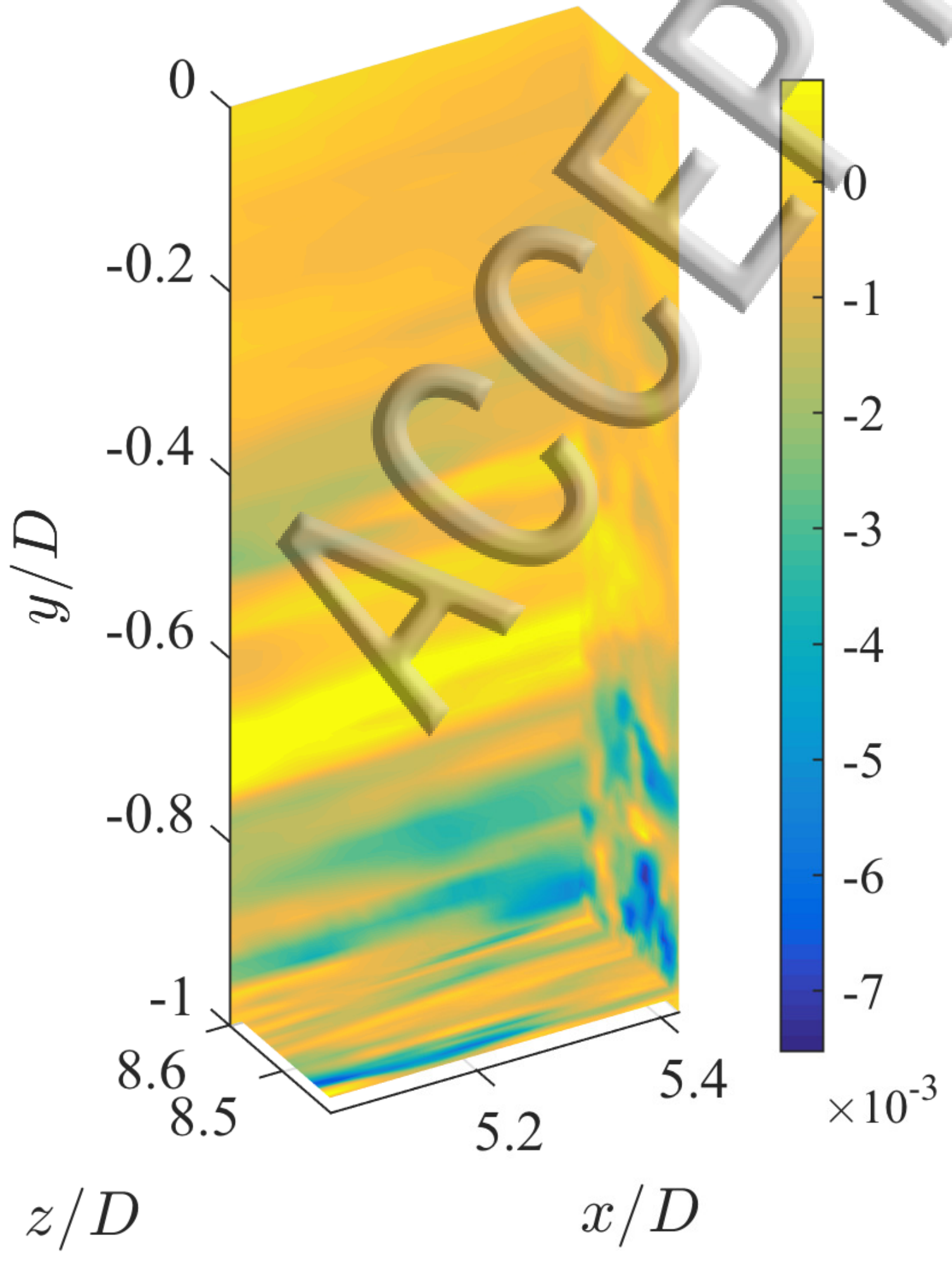

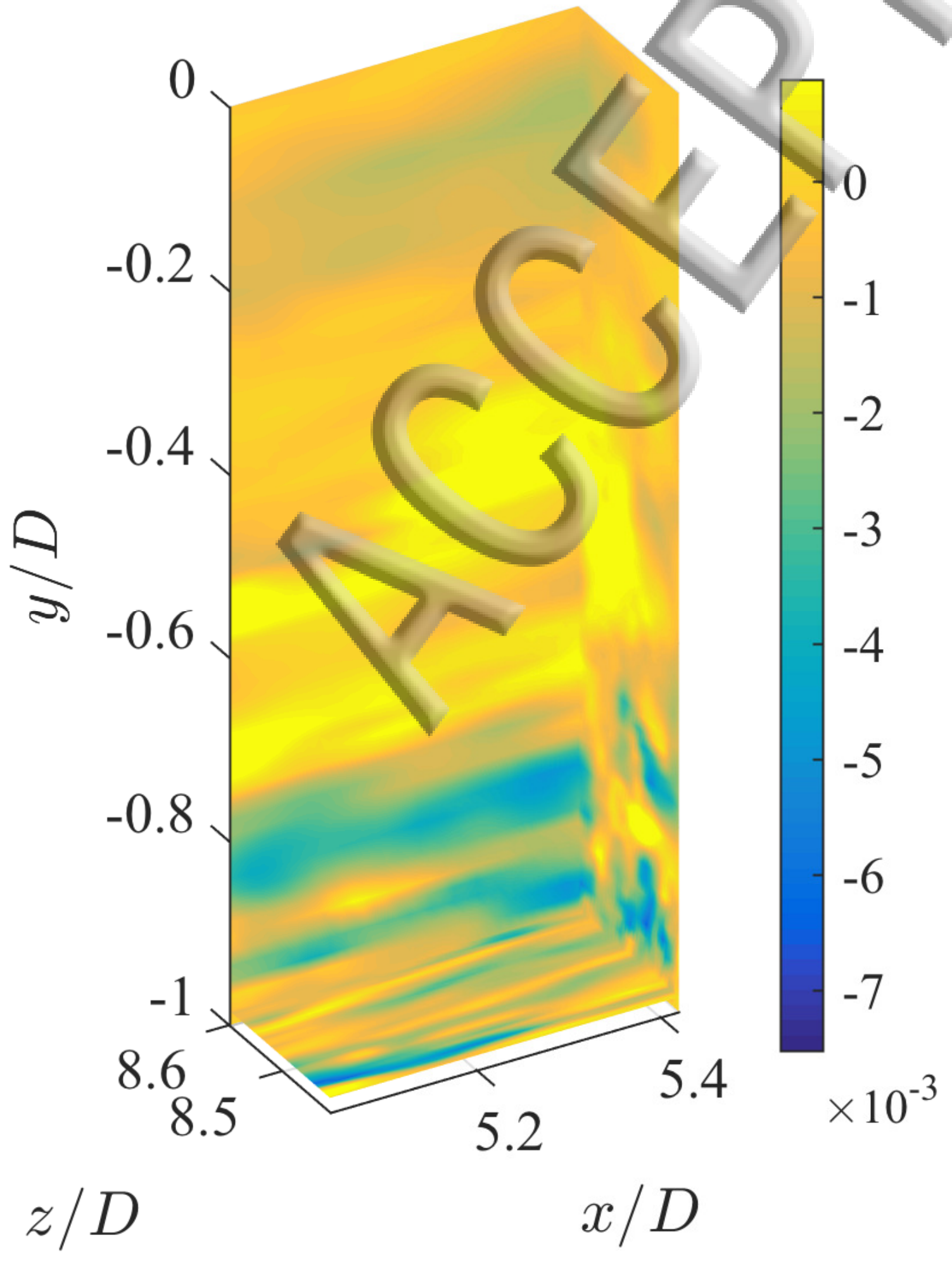

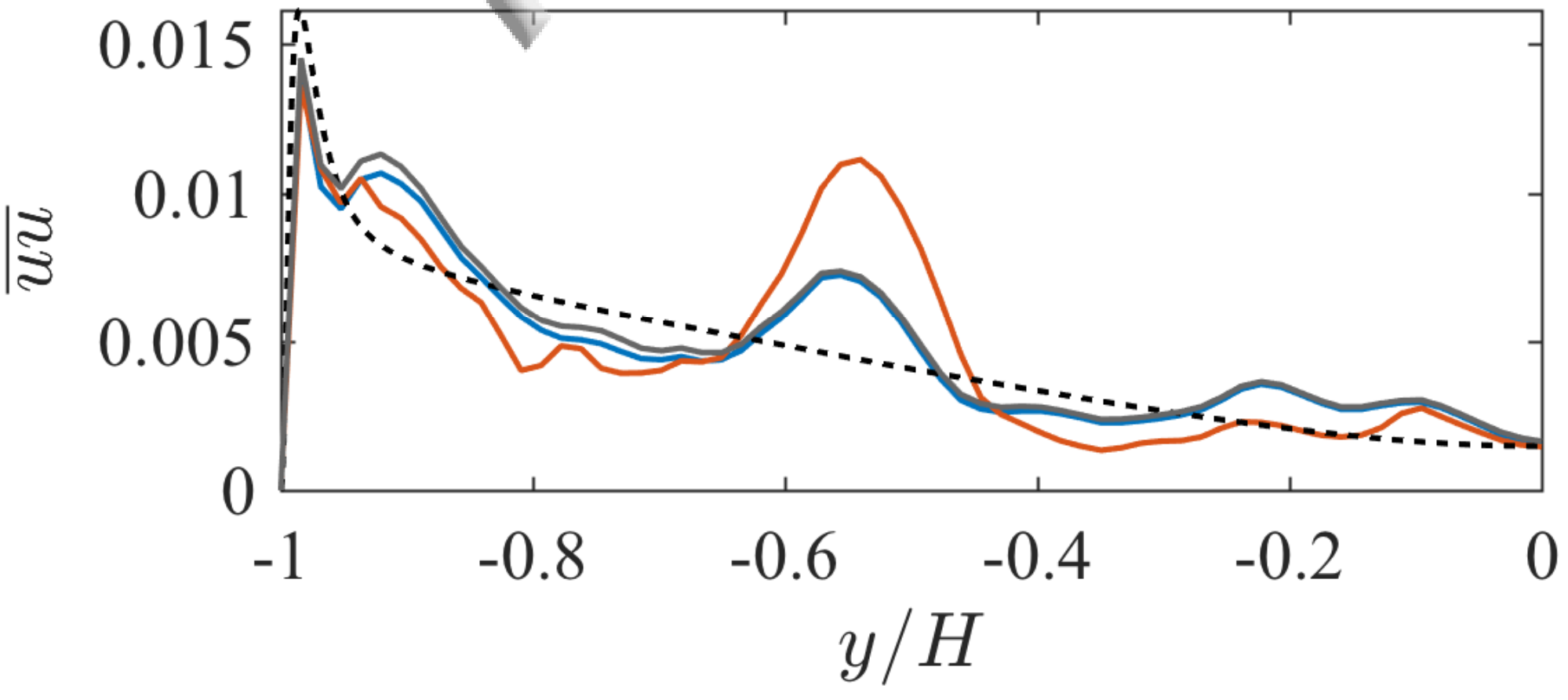
0.015
0.01
0.005
0
$\overline{uu}$
-1
-0.8
-0.6
-0.4
-0.2
0
y/H

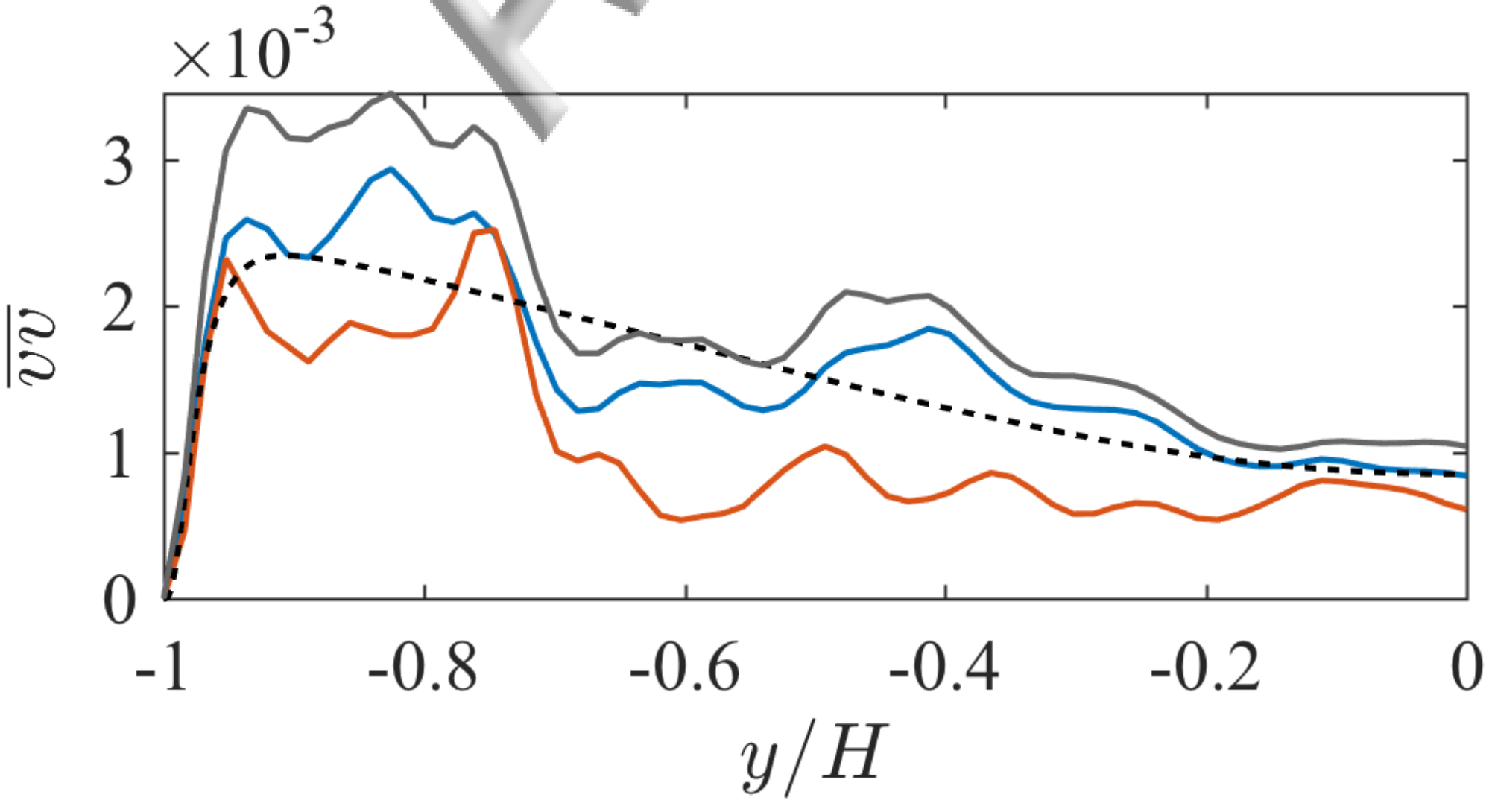
×10-3
3
2
1
0
$\overline{vv}$
-1
-0.8
-0.6
-0.4
-0.2
0
y/H

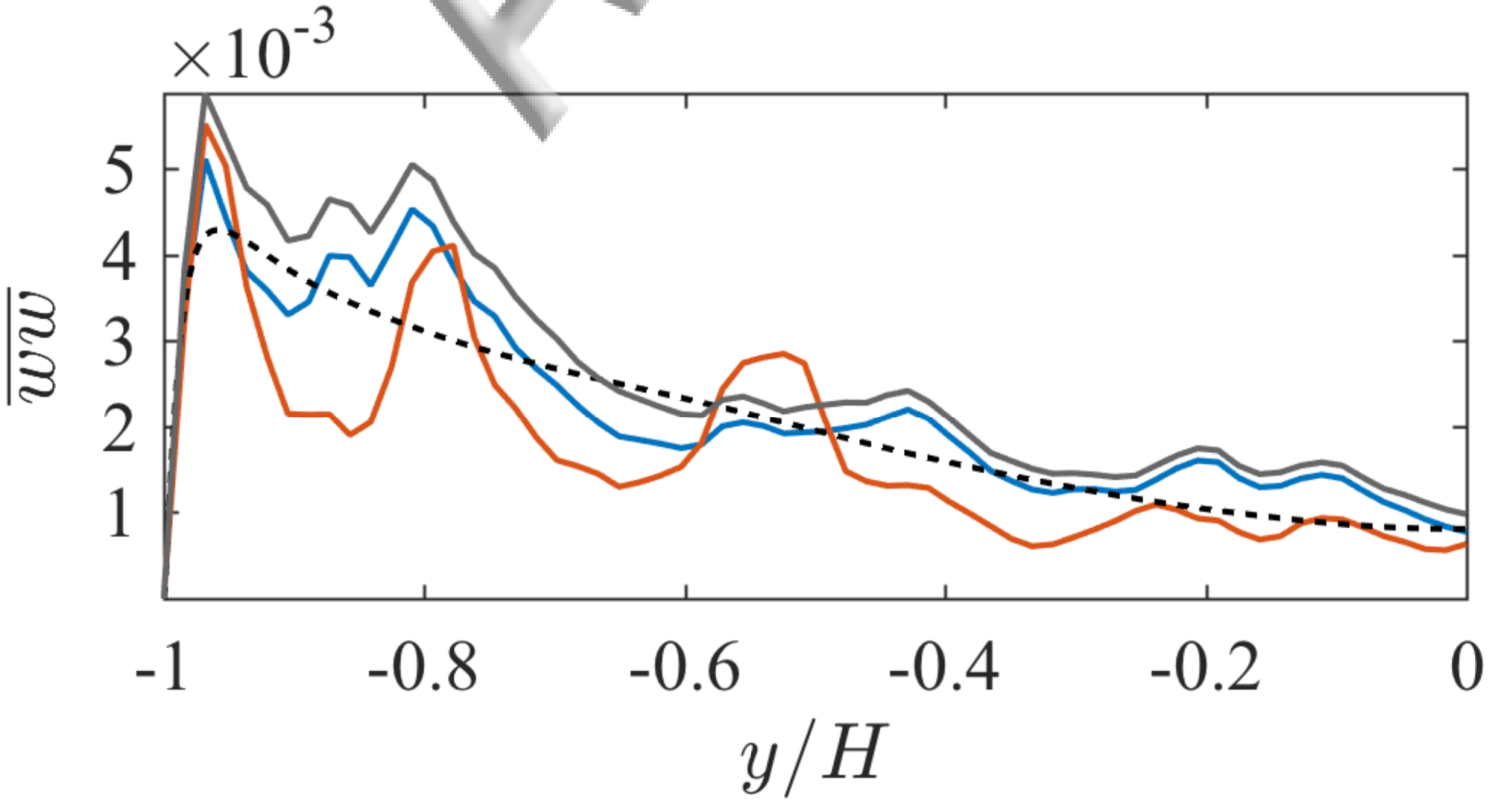
×10-3
5
4
3
2
1
$\overline{ww}$
-1
-0.8
-0.6
-0.4
-0.2
0
y/H

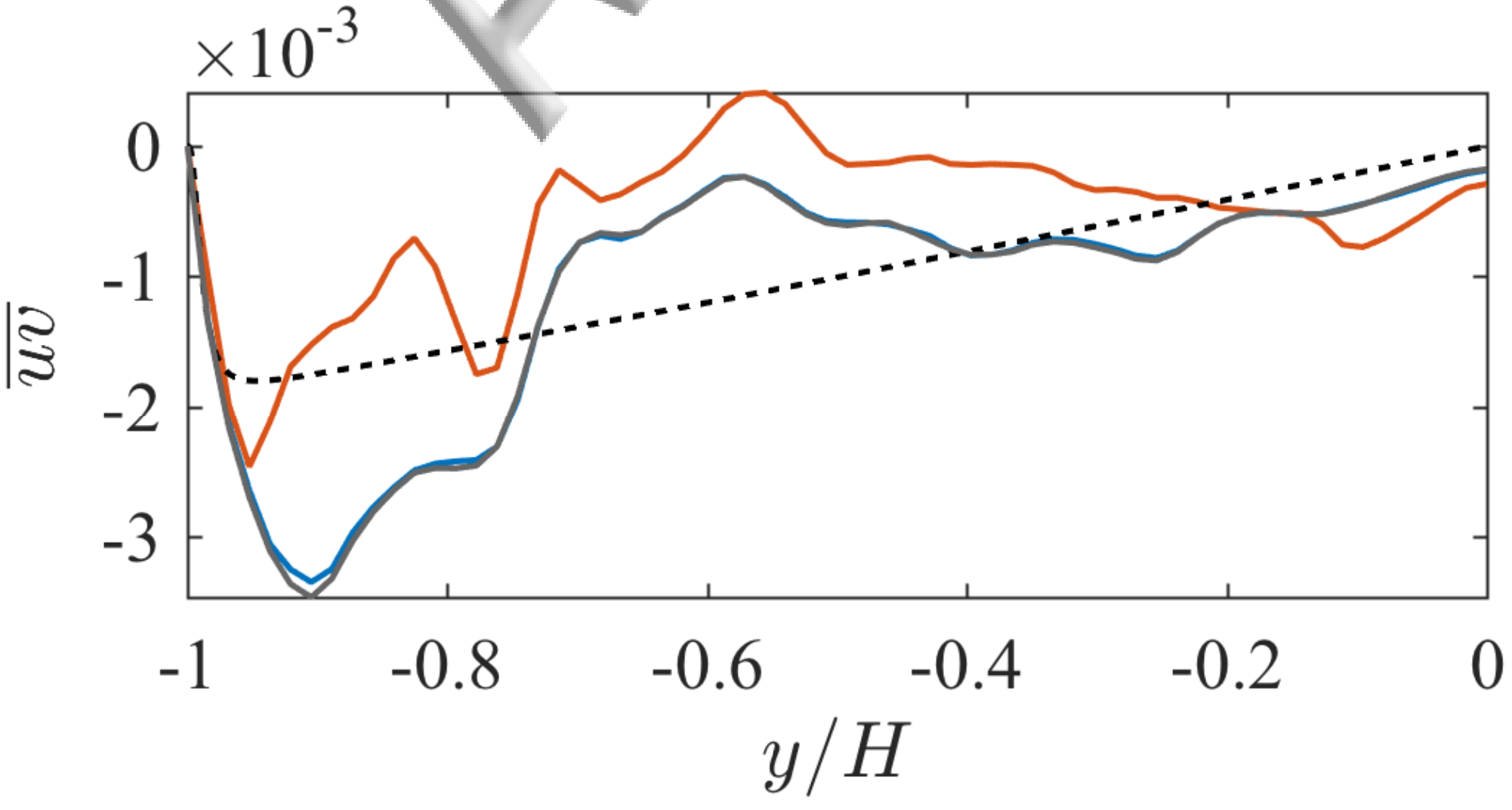
×10^-3
0
-1
-2
-3
$\overline{uv}$
-1
-0.8
-0.6
-0.4
-0.2
0
y/H

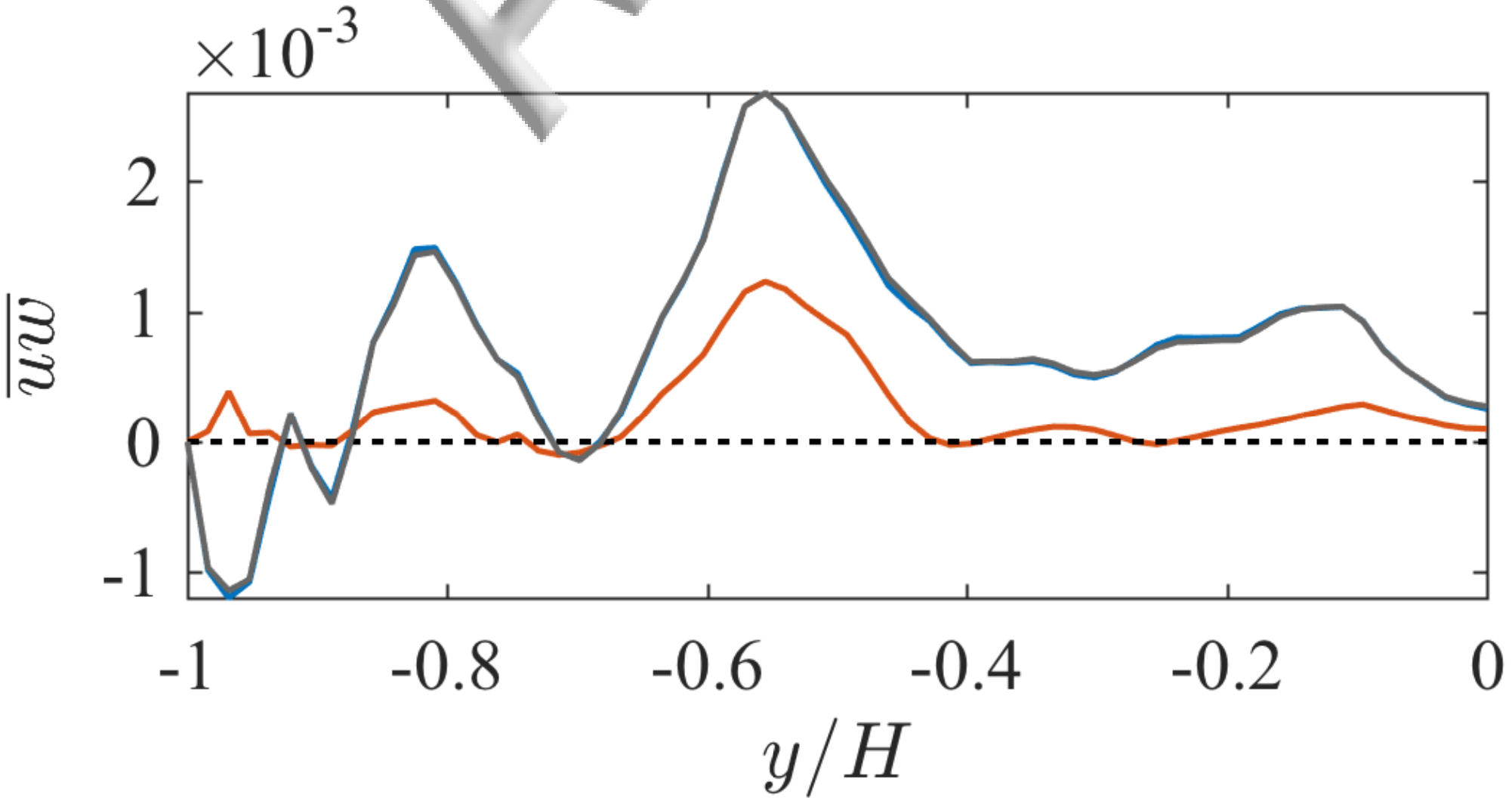
×10-3
2
1
0
-1
$\overline{uw}$
-1
-0.8
-0.6
-0.4
-0.2
0
y/H

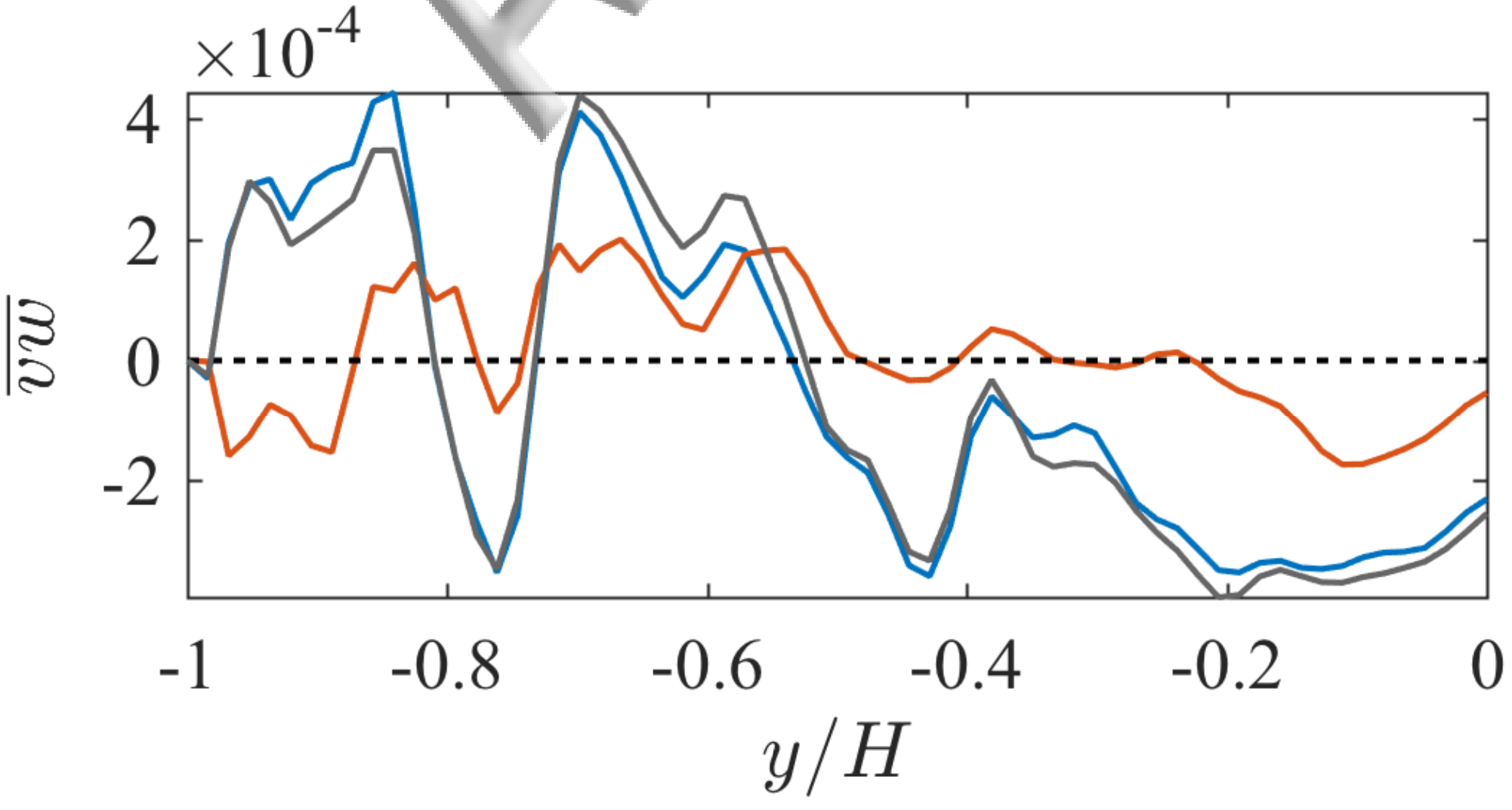
×10-4
4
2
0
-2
$\overline{vw}$
-1
-0.8
-0.6
-0.4
-0.2
0
y/H